



HAL
open science

High temperature oxidation study of direct laser deposited AlXCoCrFeNi (X=0.3,0.7) high entropy alloys

A. Mohanty, J.K. Sampreeth, Omkar Bembalge, J.Y. Hascoet, S. Marya, R.J. Immanuel, S.K. Panigrahi

► To cite this version:

A. Mohanty, J.K. Sampreeth, Omkar Bembalge, J.Y. Hascoet, S. Marya, et al.. High temperature oxidation study of direct laser deposited AlXCoCrFeNi (X=0.3,0.7) high entropy alloys. Surface and Coatings Technology, 2019, 380, pp.125028 -. 10.1016/j.surfcoat.2019.125028 . hal-03488676

HAL Id: hal-03488676

<https://hal.science/hal-03488676>

Submitted on 20 Jul 2022

HAL is a multi-disciplinary open access archive for the deposit and dissemination of scientific research documents, whether they are published or not. The documents may come from teaching and research institutions in France or abroad, or from public or private research centers.

L'archive ouverte pluridisciplinaire **HAL**, est destinée au dépôt et à la diffusion de documents scientifiques de niveau recherche, publiés ou non, émanant des établissements d'enseignement et de recherche français ou étrangers, des laboratoires publics ou privés.



Distributed under a Creative Commons Attribution - NonCommercial 4.0 International License

High temperature oxidation study of direct laser deposited $\text{Al}_x\text{CoCrFeNi}$ ($X=0.3,0.7$) High entropy Alloys.

A. Mohanty¹, J.K. Sampreeth¹, Omkar Bembalge¹, J.Y. Hascoet², S. Marya^{2, 1}, R.J. Immanuel¹, S.K. Panigrahi^{1*}

¹ Department of Mechanical Engineering,
Indian Institute of Technology Madras, Chennai- 600036, India

² Institut de Recherche en Génie Civil et Mécanique, UMR 6183,
Ecole Centrale de Nantes, 44321 Nantes, France

*Corresponding Author: Phone: +91-44-22574742, E-mail: skpanigrahi@iitm.ac.in

Abstract

High entropy alloys (HEAs) are being explored as prospective substitutes for high temperature structural components. These HEAs are typically fabricated using conventional techniques like arc melting, mechanical alloying etc., but these routes exhibit a wide range of limitations. Direct laser deposition (DLD) process (an additive manufacturing technique) generates complex products from metal powder by selectively melting alloy powder in successive layers. The present study shows the development of HEAs namely $\text{Al}_{0.3}\text{CoCrFeNi}$, $\text{Al}_{0.7}\text{CoCrFeNi}$ possessing crystal structures face-centered cubic (FCC) and FCC plus body-centered cubic (BCC) respectively using direct laser deposition (DLD) technique. HEA plates of the above-mentioned alloys were fabricated using DLD technique. In the present work, microstructures, mechanical (mainly hardness) and cyclic oxidation behaviors at 1100 °C of developed HEAs have been investigated. Microstructural studies revealed FCC and FCC+BCC structures respectively, for $\text{Al}_{0.3}\text{CoCrFeNi}$ and $\text{Al}_{0.7}\text{CoCrFeNi}$ alloys with corresponding hardness of 170HV and 380HV. Cyclic oxidation studies were performed on the HEAs at a temperature of 1100 °C for 200 h. Both the HEAs displayed quasi parabolic oxide growth after an initial sharp growth slope. Over the studied oxidation period, the mass gain for HEA $\text{Al}_{0.3}\text{CoCrFeNi}$ was greater than for $\text{Al}_{0.7}\text{CoCrFeNi}$. Each oxidized HEAs forms an external Cr_2O_3 scale with Al_2O_3 subscale formed

beneath, but the thickness and continuity of oxide layers vary according to Al content. Increased Al content enhanced the oxidation resistance of the HEA.

Keywords

A. High entropy alloys B. Additive manufacturing C. Microstructure D. Cyclic Oxidation

1. Introduction

High entropy alloys (HEAs), also known as multi-component materials, primarily comprises of at least four to five prominent mixing elements with concentration ranging between 5-35 at% [1-3]. Multiplicity of high entropy alloys leads to various properties, which are different from conventional alloys. Four 'core effects' are often used to describe HEAs: lattice distortion, sluggish diffusion, high entropy and cocktail effects. "Sluggish diffusion" was proposed as one of the core effects in HEAs. However, recent investigation by utilizing using tracer diffusion and inter-diffusion techniques has shown that the diffusion in HEAs need not be assumed sluggish. These diffusion measurements have been limited only to HEA cast alloys [3], a proper investigation for HEAs formed after mechanical alloying and consolidation through different manufacturing technique is required. Opposite to the traditional phase rule prediction, the high entropy of mixing for HEAs results in the formation of stable solid-solution phases rather than complex phase microstructures consisting of inter-metallic [3, 4] avoiding thereby the drawbacks of conventional or traditional multi-component alloys. Several studies over various high entropy alloy systems have been summarized [2, 5, 6]. Yang and Zhang [5] utilized this database to ascertain the stability of solid solution phases under some conditions: an atomic size difference ($\delta < 6.6\%$) and a factor that includes the effect of entropies and enthalpies of mixing and constituent melting points ($\Omega > 1.1$). Other investigators have associated the emergence of solid solutions in HEAs to electronegativity [7] and valence electron concentration [8].

HEAs exhibit several alluring properties such as excellent corrosion, oxidation, thermal softening and wear resistance along with high strength, hardness, ductility and low inter-diffusion. These properties are beneficial in various applications like aero-engine components,

refractory coatings, molds, tools [9-11]. The properties and the crystal structure of HEAs considerably confide in its composition and processing routes. A series of manufacturing techniques such as spark plasma sintering, vacuum arc melting, annealed cold rolling and high-pressure torsion etc., have been utilized to manufacture high performance HEAs in bulk form with considerable investment in resources and time [12-16].

HEAs have also been deposited in the form of surface coating via selective laser melting [17], welding [18, 19], direct laser deposition [20-23], additive manufacturing (AM) [24-25] and thermal spraying [26]. The aforementioned routes are most unlikely to provide an industrially suitable solution for the manufacturing and use of HEAs. HEAs are relatively a multiplex system with demanding stringent controls, where its potential interests need to overcome the inherent complexity. With this in view, it appears that AM, which expedite a superior level of localized process control and results in an accelerated solidification cooling rate, can be thought as suitable and emerging manufacturing route for HEAs as an advanced and strategic engineering material. Thus, the present work was carried out with utmost aims: to exhibit the feasibility of manufacturing HEAs via an AM route and to study the microstructure and microhardness of a five-component AlCoCrFeNi HEA produced by AM, which only a few authors have reported yet [20-25].

High entropy alloys can be used in various high temperature applications, where the oxidation behavior of the alloys becomes critical. Works have been reported on the oxidation behavior of various HEA systems [27-30]. If not all, most of the results reported on the oxidation behavior of HEA systems pertain to conventionally fabricated, i.e. non AM test specimens. Reported results in the same studies show that HEAs have higher oxidation resistance when compared to conventional alloys. However, there is no research done on oxidation of HEAs synthesized through the direct laser deposition process for a five-component AlCoCrFeNi HEA produced by AM. Taking into consideration, the emerging popularity and potential applications of the HEAs

in various fields, a study onto its oxidation behavior is required. Thus, the present research also has been carried out to elucidate the microstructures and mechanisms of oxidation in $Al_xCoCrFeNi$ HEA produced by AM.

In the present study $Al_{0.3}CoCrFeNi$ and $Al_{0.7}CoCrFeNi$ HEAs were manufactured through direct laser deposition from elemental powder mixtures. A novel two stage process was adopted to develop two types of $Al_xCoCrFeNi$ HEA systems. In the first stage, the individual powders were sieved and intelligently mixed in the planetary ball milling without balls, followed by DLD processing route on the next stage. This integrated step is a novel route established by the authors. Since the processing route is new, none of the researchers have studied any kind of analysis, including the oxidation behavior of any type of HEAs system. Therefore, the authors have tried to understand the feasibility of this integrated manufacturing route along with its impact on oxidation behavior.

Microstructural characterization study was performed to verify the crystal structures and phases formed with the existing literature. Cyclic oxidation tests were performed on the synthesized HEAs to study their oxidation behavior at high temperature. The research also presents and compares the microstructure growth of two HEAs developed during oxidation at 1100 °C. Oxidation mechanisms are also postulated and discussed.

2. Experimentation

The HEAs with nominal compositions of $Al_xCoCrFeNi$ ($x=0.3$ and 0.7) i.e. $Al_{0.3}CoCrFeNi$ and $Al_{0.7}CoCrFeNi$ were fabricated using direct laser deposition (DLD). A DLD apparatus was used for synthesizing $Al_xCoCrFeNi$ HEAs from elemental powder: Al, Co, Cr, Fe and Ni (Jedee enterprise Mumbai, purity >99%, size varying from 30-120 μm).

The commercially purchased powders are of random shapes and their sizes vary in the range of around 30-120 microns. Initially, all the five powders were sieved individually in a planetary ball mill (model no. DECO-PBM-V-2L-C). Thereafter, powder mixtures were prepared in a planetary

ball mill without the use of high energy balls in order to avoid powder size reduction and mechanical alloying. All the five elements were weighed in specific proportions and powder mixtures were prepared in such a way that they form $Al_{0.3}CoCrFeNi$ and $Al_{0.7}CoCrFeNi$ blends.

This prepared blend were again sieved in a planetary ball mill to maintain uniformity of the powder mixture.

Fig. 1 represents the blended powder along with its EDS, showing that the powders are more or less uniformly mixed and distributed within the powder mixture. These powder mixtures were then passed through a hopper system at a feed rate of 1.5 g/min, scan rate of 15 mm/s and under the laser powers of 350 W for the first two layers, 300 W for the next two layers and 250 W for further layers. The HEAs were deposited on a stainless-steel substrate of 5 mm thickness. The dilution from the first deposits on the base stainless steel was negligible, even though higher laser power was used, and wasn't passed over to the successive build layers. It may be mentioned that a higher laser power (350W) in the first layer was required to make the first layer stick to the cold substrate.

Microstructural analysis was done on both HEA samples. Sample of width 1 cm were cut from the parent samples for the analysis. The samples were cut in a direction perpendicular to the direction of processing. The cut samples were initially ground aggressively using silicon carbide (SiC) 400 to 3000 emery grades, followed by 1 μ m diamond abrasive paste at the end. Samples were electro-polished using an electrolyte whose composition was 80% methanol and 20% perchloric acid. Electro polishing was carried out under a voltage of 15 V for a period 30 seconds. SEM system equipped with secondary electrons (SE)/ backscattered electrons (BSE), energy dispersive X-ray spectroscopy (EDS) and electron backscatter diffraction (EBSD) detectors was used for microstructural characterization and chemical composition analysis of HEA samples.

X-ray diffraction (XRD) profiling was performed for determining the phases of HEAs. The crystallographic phases were identified using monochromatic Cu (K-alpha) radiation over a scanning range of $20^\circ < 2\theta < 90^\circ$.

The hardness of the samples was determined using the microhardness instrument (Vickers test). The test load used for measuring hardness was 500 gf for dwell time of 15 seconds. The hardness was measured in such a way that hardness is calculated along all the additive manufactured layers. The hardness was measured at 30 different points on each sample along two sections, with 15 points in each section.

A cyclic oxidation test was carried out on both HEA samples in static air at 1100 °C in an alumina tubular furnace. The total oxidizing time of 200 hours was considered to be adequate to allow steady state oxidation. Each cycle consisted of 10-hour heating at 1100°C followed by 20 minutes cooling time at room temperature. Both the HEA samples were polished with 1000 grade emery paper followed by 2000 grade emery paper and cleaned with ethanol to remove the grits. Prior to oxidation test, the dimensions of the samples were measured using digital Vernier callipers having least count of 0.01 mm to compute their surface areas. Then both the HEA samples were placed in alumina boats which were cleaned with ethanol to remove the dust particles. Prior to placing the samples in tubular furnace, weighing of the samples was done along with alumina boats. The successive weighing of the samples was done along with the boat to take the spilled scales into the consideration for the weight change measurements. Further, thermogravimetric analysis (TGA) test was carried out by using Perkin Elmer DSC in order to analyze the effect of Al content on the oxidation resistance of $\text{Al}_x\text{CoCrFeNi}$ ($X=0.3,0.7$). For this, both HEAs were heated from room temperature to 1100°C under the normal atmosphere at a heating rate of 20 °C/min.

The surface of oxidized samples was analyzed by SEM at various intervals. The samples were also examined by XRD. The cross-section of the oxide scales formed was analyzed through SEM. The phases formed during oxidation were characterized by XRD.

3. Results

3.1 Phase Constitution and Microstructural analysis

The XRD patterns of two HEAs manufactured by the AM route are shown in Fig. 2. Peaks corresponding to the FCC and BCC were identified. The XRD spectra for low Al content HEA ($\text{Al}_{0.3}\text{CoCrFeNi}$), showed formation of a FCC phase. Whereas, the incorporation of more Al effectively stabilizes the BCC structure, thereby generating a duplex FCC+BCC phase in $\text{Al}_{0.7}\text{CoCrFeNi}$ alloy. The phase analysis in this study is in accordance with other investigations pertaining to similar alloys synthesized using arc melting [12-13] and laser processing [20-25].

Representative SEM images of both HEA produced by DLD are shown in Fig. 3. The FCC $\text{Al}_{0.3}\text{CoCrFeNi}$ solid solution alloy exhibited a coarse columnar structure, as can be clearly observed from Fig. 3 (a). The image clearly reveals that a single FCC solid solution phase is formed. The SEM morphology of FCC-BCC $\text{Al}_{0.7}\text{CoCrFeNi}$ alloy i.e. Fig. 3 (b), phase contrast appears in the image indicating that two phases are formed. SEM morphology indicted generation of a coarse dendritic grain structure with the primary growth arm perpendicular to the direction of laser scan. The coarse dendritic grain structure consisted of FCC phase in the dendrites and BCC phase distributed in the inter-dendritic region.

SEM-EDS was utilized to qualitatively investigate the compositional distribution across the microstructure of both HEAs. Fig. 4 and Fig. 5 displays EDS for both HEAs. From both the figures, it can be observed that elements such as Al, Co, Fe, and Cr more or less verify with the ideal atomic percentage while atomic percentage of Ni in the HEA appears more than that in the ideal case. The powders as shown in Fig. 1 did not have optimized morphology, i.e. spherical. Of

all powders, Ni had a near uniform grain distribution between 30 to 80 microns. Preliminary experiments with the blended powders showed the impossibility of fabricating the walls due to the large spectrum of powder grains. The powders clogged the nozzle and the overall flow of the powders was erratic. The powder blends were then sieved to 30-90 microns, leaving smaller and bigger particles of powder outside the usable range. This concerned mostly powders of Fe, Al, Cr, CO. This probably reduced the amount of Al, Fe, Cr, Co in the composition of walls with subsequent higher Ni contents.

The white region in Fig. 3 (b) and Fig. 5 i.e. on the EDS of $\text{Al}_{0.7}\text{CoCrFeNi}$ corresponds to FCC phase, whereas the darker region correlates to BCC phase. The EDS for white region indicated by spot 4 in Fig. 5 displayed higher amount of Cr, Co and Fe. Whereas corresponding to this the EDS of the darker region i.e BCC phase (Spot 3, Fig. 5) is enriched in Al and Ni. Cr and Al displayed the most significant segregation to FCC and BCC phases respectively. The range/amount of composing elements in both phases can be observed from Fig. 7, EDS elemental map of $\text{Al}_{0.7}\text{CoCrFeNi}$.

The Fig. 6 and Fig, 7 represents an elemental mapping of the HEA $\text{Al}_{0.3}\text{CoCrFeNi}$ and $\text{Al}_{0.7}\text{CoCrFeNi}$ respectively. Elemental maps give us the information about the distribution of elements in the high entropy alloy. Elemental mapping images show the distribution of all the elements and then the distribution of individual elements within the alloy. Fig. 6 reveal that all the elements are distributed uniformly within the region for and there is no coagulation of elements at any place within the alloy. Hence, indicating formation of single phase, i.e. FCC in HEA $\text{Al}_{0.3}\text{CoCrFeNi}$. With an increase of the Al content from 0.3 to 0.7, a small fraction of intercellular BCC phase was observed in the FCC matrix due to solidification segregation of Al and Ni, as seen from Fig. 7.

Figure 8 corresponds to EBSD analysis of both of the high entropy alloy sample. EBSD scans revealed that there is a proper diffusion in between the consecutive deposited layers. Both HEAs

have been developed through the AM route, where alloy powders were selectively melted in successive layers to generate bulk component. But still due to proper diffusion of multi-component alloy powder during the manufacturing process, it's hard to distinguish successive layers. This illustrates one of the advantages of using AM as a processing route for HEAs. Fig. 8(a) displays the EBSD scan of $Al_{0.3}CoCrFeNi$. The alloy appears to have long elongated grains oriented in the direction of $\langle 001 \rangle$. Fig. 8(b) shows the EBSD scan of $Al_{0.7}CoCrFeNi$. This alloy also appears to have long elongated grains, but an equal number of grains oriented in different directions, i.e. $\langle 001 \rangle$, $\langle 111 \rangle$ and $\langle 101 \rangle$.

The variation of hardness values along the layer by layer deposited direction is represented in the Fig. 9. The measured hardness of $Al_{0.3}CoCrFeNi$ was lying in the range of 140HV-205HV, with an average hardness of around 170HV, Fig. 9 (a). Similarly, for the alloy $Al_{0.7}CoCrFeNi$ the hardness was found to be in between 262HV-509HV. The average value of hardness was around 380HV, Fig. 9 (b).

3.2 Oxidation Study

3.2.1. Oxidation Kinetics

The oxidation rates of both HEAs were calculated at $1100^\circ C$ in static air for 200 h. Fig. 10 displays normal mass gain (mg/cm^2) curve and as well parabolic plot during cyclic oxidation at $1100^\circ C$. As observed, the mass changes for HEA $Al_{0.3}CoCrFeNi$ increased with duration. Whereas HEA $Al_{0.7}CoCrFeNi$, exhibited initial mass gains that slowed down with time. The mass gain for HEA $Al_{0.3}CoCrFeNi$ and $Al_{0.7}CoCrFeNi$ at the end of 200 h are found to be $1.1 mg/cm^2$ and $0.485 mg/cm^2$ respectively. Clearly from Fig. 10 (a), the mass gain for HEA $Al_{0.3}CoCrFeNi$ was observed to be higher as compared to $Al_{0.7}CoCrFeNi$ during the entire duration of oxidation study. Hence, better oxidation resistance at $1100^\circ C$ in static air for 200 h was found with HEA $Al_{0.7}CoCrFeNi$ as it had quite low overall mass gain. It is evident from the

plot that the both HEAs initially followed a transient stage, with subsequent parabolic behavior thereafter. An analysis of mass gain curves suggests that no trace of spallation of oxides during the measurement, as there was no notable drop-offs on the mass gain curve during the cyclic oxidation. Fig. 11 shows thermogravimetric analysis (TGA) for both HEA $\text{Al}_{0.3}\text{CoCrFeNi}$ and $\text{Al}_{0.7}\text{CoCrFeNi}$. In TGA, the weight of both HEAs was measured over time as the temperature changed from room temperature to 1100°C . It can be observed from Fig. 11, that weight gain for HEA $\text{Al}_{0.3}\text{CoCrFeNi}$ (0.08488 mg) is nearly 27% higher than that of $\text{Al}_{0.7}\text{CoCrFeNi}$ (0.06193 mg). Hence, TGA analysis also proves that oxidation resistance for HEA $\text{Al}_{0.7}\text{CoCrFeNi}$ to be superior as it had quite low weight gain compared to HEA $\text{Al}_{0.3}\text{CoCrFeNi}$.

The parabolic rate constants K_p was determined from the slopes of $(\Delta W/A)^2$ versus time (t) Fig. 10 (b), where $\Delta W/A$ is the mass gain per unit area, and t is the oxidation time in seconds. The K_p value for the HEA $\text{Al}_{0.3}\text{CoCrFeNi}$ and $\text{Al}_{0.7}\text{CoCrFeNi}$ are 1.7×10^{-12} and 3.8×10^{-13} respectively. It can be observed that the higher Al content HEA $\text{Al}_{0.7}\text{CoCrFeNi}$ resulted in the lower value of K_p as compared to HEA $\text{Al}_{0.3}\text{CoCrFeNi}$. K_p can be considered as a measure of oxidation resistance for any alloy, a lower value signifies higher protection to oxidation. Table 1 summarizes the values of K_p for different high entropy as well conventional alloys obtained by various researchers [28,30]. The oxidation kinetics i.e parabolic constant of both AM HEAs was lower than that of other HEAs developed by various researchers through conventional routes.

3.2.2. Oxide Scale Morphology

Fig. 12 and Fig. 13 displays the surface morphology of various oxide scales formed on the surface of HEAs $\text{Al}_{0.3}\text{CoCrFeNi}$ and $\text{Al}_{0.7}\text{CoCrFeNi}$ respectively, oxidized at 1100°C for different duration. SEM micrographs of oxide scales for $\text{Al}_{0.3}\text{CoCrFeNi}$ (Fig. 12) displays an irregular characteristic with a plenty of nodules and rough oxide crystallites formed on the

surface. However, SEM micrographs of the oxide scale morphology developed on $\text{Al}_{0.7}\text{CoCrFeNi}$ (Fig. 13) were dissimilar than that developed on $\text{Al}_{0.3}\text{CoCrFeNi}$ surface. The oxide scales formed were dense, with fine polyhedral oxide crystallites.

The EDS analysis of the scale of both HEAs after 20 h duration, Fig. 12 (a) & 13 (a) shows oxides of Cr and Al as the main constituents and supports the possibility of formation of spinels of mixed oxides due presence of small amount of Ni, Fe and Co. The black region on a scale indicates formation of Al_2O_3 , whereas white region indicates Cr_2O_3 oxide layer on the oxidized surface. With the increase in duration, the surface of the oxidized sample for both HEAs is covered with higher amount of Cr_2O_3 oxide scale while the Al_2O_3 oxide decreases Fig. 12 (b) & 13 (b). This indicates the formation of several layers of oxides on the surface with Cr_2O_3 oxide being formed as an external layer while Al_2O_3 as an internal layer beneath Cr_2O_3 oxide scale. Comparatively higher percentage of Cr_2O_3 oxide scales are formed on the oxidized $\text{Al}_{0.3}\text{CoCrFeNi}$ (Fig. 12 (c)) surface than that developed on the surface of $\text{Al}_{0.7}\text{CoCrFeNi}$, Fig. 13 (c).

3.2.3 Cross-section morphology of oxide scales

Fig. 14 (a-c) represents cross-sectional SEM micrographs of the oxide scale morphology developed on $\text{Al}_{0.3}\text{CoCrFeNi}$ at 1100°C for 20, 100 and 200 h respectively. **Based on inspection, the $\text{Al}_{0.3}\text{CoCrFeNi}$ formed an external Cr_2O_3 oxide layer along with a discontinuous Al_2O_3 internal subscale.** As observed in Fig. 14 (a), after 20 h of oxidation, an intermittent outward Cr_2O_3 oxide layer developed on the $\text{Al}_{0.3}\text{CoCrFeNi}$ HEAs surface along with an interior subscale composing of coarse Al_2O_3 precipitates. With duration, the thickness of the external Cr_2O_3 oxide layer and coarsening of Al_2O_3 precipitates increased as can be noticed from Fig. 14 (b-c). Fig. 14 (c) shows the EDS quantitative analysis of cross-section morphology for $\text{Al}_{0.3}\text{CoCrFeNi}$ at various locations. EDS analysis clearly reveals the top scale to be rich in Cr and O, indicating the

formation of Cr_2O_3 oxide layer. Whereas, subscale was enriched in Al and O. Below the subscale of Al_2O_3 , an Al and Cr depleted region existed.

Fig. 15 displays representative SEM images of cross-section morphology for $\text{Al}_{0.7}\text{CoCrFeNi}$ after oxidation at 1100°C for 20, 100 and 200 h respectively. SEM micrographs of oxidized HEA after 20 h (Fig. 15 a) exhibited a thin discontinuous layer of Cr_2O_3 oxide along with minor Al_2O_3 precipitates. After 100 h duration, the Al_2O_3 precipitates coarsened highly, with an indication of the formation of a thick layer on further oxidation, as observed from (Fig. 15 b). Upon further oxidation the coarsened Al_2O_3 precipitates developed into a continuous thick layer beneath a thin external Cr_2O_3 scale after 200 h of oxidation, as shown in (Fig. 15 c). EDS analysis clearly reveals the thin top scale to be rich in Cr and O, indicating the formation of Cr_2O_3 oxide layer. Whereas, thick subscale was enriched in Al and O. Below the subscale of Al_2O_3 , an Al depleted region existed, but high enough Al concentration (5.95 at. %) in its composition to further form Al_2O_3 . High amount of Al present in the $\text{Al}_{0.7}\text{CoCrFeNi}$ HEA lead to the formation of a thick Al_2O_3 oxide layer, which provided superior oxidation resistance in comparison to low Al content $\text{Al}_{0.3}\text{CoCrFeNi}$ HEA.

3.3.4. Phase Analysis by XRD

XRD analysis was also performed to identify phases formed in both HEAs after the cyclic oxidation test. XRD patterns of the $\text{Al}_{0.3}\text{CoCrFeNi}$ and $\text{Al}_{0.7}\text{CoCrFeNi}$ HEA after cyclic oxidation after 20 h and 200 h duration of oxidation are shown in Fig. 16. For $\text{Al}_{0.3}\text{CoCrFeNi}$ HEA its FCC, Cr_2O_3 , Al_2O_3 , NiO and NiCr_2O_4 spinel peaks are observed. Whereas, in case of $\text{Al}_{0.3}\text{CoCrFeNi}$, an additional peak of BCC phases was observed.

4. Discussion

4.1. Microstructure of additive manufactured HEAs

Additive manufacturing (AM) is a complex net-shaping method. It involves a processing technique which follows from a 'line' to a 'layer' and then to a 'bulk'. AM initially begins with a single line scanning, these multiple scan lines produce a layer. Then layer by layer deposition leads to bulk formation of material. The densification extent is an elemental feature that decides various mechanical properties of AM produced components. Near full density parts made from metals, alloys and blended/composite powders can now be manufactured under the optimized processing parameters. Hence, optimized parameters were selected during additive manufacturing of both high entropy alloys in the present study. The bulk formation of HEAs through AM route in the present study, was obtained via layer by layer deposition. No cracks or pores were formed in the manufactured HEA components. Similar observation can also be made from Fig. 3, i.e. EBSD analysis of two high entropy alloys $Al_{0.3}CoCrFeNi$ and $Al_{0.7}CoCrFeNi$. EBSD scans reveal that there is a proper diffusion in between the consecutive deposited layers. It is difficult to identify interface between the two consecutive deposited layers. In general, fast quenching becomes necessary as HEA may endure different phase changes while steady cooling owing to decrement in the thermodynamic driving force at modest temperatures. Additionally, the expeditious quenching rate regulates the diffusion process of elements and hence, hinders nucleation and generation of the brittle intermetallic compounds, thereby retaining the HEA phases. The XRD patterns of additive manufacturing HEAs (Fig. 2) clearly demonstrates the above. These all clearly demonstrate the AM as an efficient method for manufacturing HEA in bulk form.

The microstructural variation of the $Al_xCoCrFeNi$ HEA system can be elucidated by phase change occurred due to lattice distortion [31]. The strain generated in lattice ' ϵ ' can be demonstrated by:

$$\varepsilon = |a - a_0| / a_0$$

Where, 'a₀' and 'a' are the lattice constant for perfect crystal and actual alloy without distortion. Because of higher atomic radius of Al, the strain in lattice notably rises with Al inclusion. As BCC is not a closely pack structure, it is likely that phase change from initial FCC to BCC happens to minimize the lattice distortion generated by a mismatch in the atomic size of the composed elements. In the present investigation, Al_{0.3}CoCrFeNi HEA revealed only single FCC phase. But with the inclusion of Al, a combination of both FCC and BCC phases formed. Additionally, Guo et al. [7] suggested an empirical condition for phase stability of HEA on the basis of the atomic mismatch (δ), valence electron concentration (VEC) and the electronegativity difference ($\Delta\chi$) and deduced that VEC imparted the optimum evidence for stability of various phases. VEC estimates that single FCC phase forms for VEC ≥ 8 whereas, only the BCC phase would exist for VEC < 6.68 and FCC+BCC co-exists for the intermediary VEC range. The above mentioned stability criterion are calculated and correlated with other HEAs in the prior studies, Fig. 17.

In the present study, a moderate laser beam scanning speed of 15 mm/s was considered in order to provide proper mixing of various elemental phases formed metal pool under the laser beam. In comparison with conventional casting and arc melting methods, the above scanning speed can still be considered for much higher solidification rates. A decrement in grain size is to be expected at such elevated solidification rates, resulting in an increase of microhardness [24, 32, 33]. Previous literatures have observed that microhardness of samples formed by AM to be higher than that of conventional methods such as casting and arc melting [21,22].

The average microhardness of Al_{0.3}CoCrFeNi was observed to be around 170HV, Fig. 9 (a). With the increase in Al content, the average microhardness of HEA increased. The average microhardness of Al_{0.7}CoCrFeNi was found to be around 380HV, Fig. 9 (b). The Al_{0.3}CoCrFeNi alloy possesses a FCC crystal structure making it less resistant towards localized plastic

deformation thereby showing lower hardness, whereas $\text{Al}_{0.7}\text{CoCrFeNi}$ alloy possess a FCC+BCC structure. The BCC structure consists of reduced number of dislocation slip systems compared to FCC phase. The formation of the additional BCC phase imparts hardness in the alloy formed.

Previous studies concluded that, this rise in hardness is because of the addition of Al, which results in severe lattice distortion due to its large atomic size [34] and larger negative enthalpy of mixing [35] associated with it. Among all elements, the atomic size of Al is largest. The addition of Al inevitably precedes to distortion of the lattice. The strain energy related to lattice distortion increases the overall free energy of the HEA lattice. This lattice distortion further restricts the movement of dislocations and also results in a noticeable solid solution strengthening effect. It is well familiar that the chemical blending enthalpy of Al-Cr, Al-Fe, Al-Co and Al-Ni are -6, -10, -24 and -30 KJ/mol respectively. Whereas, the mixing enthalpy for Co-Ni, Ni-Fe, Co-Fe, Cr-Fe, Cr-Co and Cr-Ni are 17, 12, 13, 13, 8 and 3 KJ/Mol respectively [7]. The above data indicates that the collaborative force of Al element with other elements is substantially higher with respect to the collaborative force of other elements in HEA. The distortion of HEA lattice and augmentation of bond strength of Al with other elements in HEA possibly results in increased hardness.

4.2. Oxidation Mechanism of HEAs

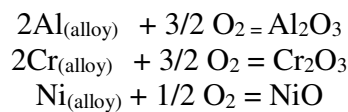
Alloys that are purposefully utilized in high-temperature oxidizing conditions solely depends on the generation of an exterior oxide scale, which imparts resistance to hot corrosion and oxidation.

This oxide scale to be beneficial, it must be thermodynamically, chemically and mechanically stable. Traditionally, these highly oxidation tolerant alloys have been composed to configure slow developing, adherent and continuous scales containing Al_2O_3 , Cr_2O_3 etc. oxide scales. Most commercially available nickel based superalloys have been developed to generate Al_2O_3 oxide scales. These oxide scales emerge steadily at slower rates, are thermodynamically stable, and

renders much superior protection in aggressive environment than that of Cr₂O₃ oxide scale. In contradistinction, the heat resistant stainless steels that are popularly used for chemical processing and energy production are designed to form Cr₂O₃ oxide scale [36,37]. It's been already outlined that high entropy alloys exhibit superior protection to oxidation and corrosion as compared to conventional alloys [38]. This improved resistance can be ascertained to tendency of HEAs towards slower diffusion property, enhanced damage tolerances and higher composition of oxide-generating elements.

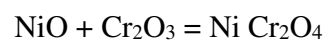
Upon oxidation of HEA Al_xCoCrFeNi consisting of five different elements, may result in the initial formation of nuclei comprising of all elements, probably metal oxides: NiO, Cr₂O₃, CoO, Al₂O₃, Fe₂O₃ and with the possible evolution of spinels: NiCr₂O₄, NiAl₂O₄ on the oxidized specimen surfaces. The thickness and durability of these oxide layers depend mostly on chemical composition and environmental condition.

XRD patterns of the oxide scale formed on the surface of oxidized Al_{0.3}CoCrFeNi (Fig. 16 a and 16 b) after cyclic oxidation in air at 1100 °C exhibits phases of metal oxides: Al₂O₃, NiO and Cr₂O₃ along with formation of mixed spinel-type oxides of NiCr₂O₄. The major oxides being Cr₂O₃ and Al₂O₃ with other oxides found to be minor amount. Upon exposure to atmosphere at high temperature, three reactions occur on the surface of Al_{0.3}CoCrFeNi HEAs:



In the beginning, Al oxidizes to Al₂O₃ before any other element due to relatively high negative free energy of formation of oxides. This leads to the formation of internal Al₂O₃ oxide scale during the start of oxidation. The EDS analysis and line scan on a surface oxide scale of Al_{0.3}CoCrFeNi HEA after 20 h duration, Fig. 18 shows oxides of Cr and Al as the main constituents and supports the possibility of formation of NiO and spinels of mixed oxides due

presence of small amounts of Ni. The black region of oxide scale indicates formation of Al_2O_3 which being internal layer, whereas white region indicates Cr_2O_3 oxide layer on the oxidized surface. The XRD pattern of such HEAs also shows the presence of mixed spinel-type oxides of NiCr_2O_4 upon oxidation. The oxide particles of Cr_2O_3 become integrated into the NiO oxide scale, reacting with the surrounding oxides. This results in the dissolution of Cr ions into the NiO lattice until either saturation of the NiO with Cr ions and the emergence of NiCr_2O_4 , given by following equation:



These metal oxides and spinel nuclei get scattered all over the HEAs surfaces, due to their fast formation, need not to be in equilibrium with the HEA. As oxidation proceeds, the further development and stability of various oxide layers generated much depends upon the composition of the HEAs. **Due to the high negative free energy of Al, initially it oxidizes easily than other elements.** But these oxides (Al_2O_3 scales) emerge steadily at slower rates and are thermodynamically stable than any other oxide formed. **Further, the presence of lower amount of Al in $\text{Al}_{0.3}\text{CoCrFeNi}$ HEA prevents selective oxidation of Al which retards the oxide growth and prevents the formation of continuous oxide layer of Al_2O_3 .** This is evident from the cross-sectional SEM micrographs of the oxide scale morphology developed on $\text{Al}_{0.3}\text{CoCrFeNi}$, indicating formation of precipitates of Al_2O_3 oxide scale, which thickened with further oxidation. With Cr been having second highest negative free energy of formation and Al acts as a “getter” resulting in the formation of a thick layer of Cr_2O_3 oxide scale. Al acts as a “getter” for oxygen by oxidizing internally to form Al_2O_3 . Hence, enabling the Cr to diffuse up to the $\text{Al}_{0.3}\text{CoCrFeNi}$ HEA surface to give an external layer of Cr_2O_3 oxide scale. With an increased oxidation duration, subsequent depletion of Al below the oxide scale and as well the selective oxidation of Cr were further enhanced. This results in almost all of Cr below the oxide scale to diffuse into the HEAs surface to form a thick continuous layer of Cr_2O_3 oxide scale in $\text{Al}_{0.3}\text{CoCrFeNi}$ HEA,

as evident from Fig. 14 (b) and (c). The high concentration of nuclei on HEA surface and negative free energy of both Cr_2O_3 and Al_2O_3 prevented other oxides from dominating the oxidation behavior.

The XRD results of $\text{Al}_{0.7}\text{CoCrFeNi}$ HEA (Fig. 16 c and 16 d) reveal the presence of various phases such as Al_2O_3 , NiO and Cr_2O_3 along with formation of mixed spinel-type oxides of NiCr_2O_4 . The early oxidation behavior of $\text{Al}_{0.7}\text{CoCrFeNi}$ HEA i.e. at 20 h of duration was found to be similar to that of $\text{Al}_{0.3}\text{CoCrFeNi}$ HEA. This can be corroborated through Fig. 19, which shows the EDS analysis and line scan on an oxide scale of $\text{Al}_{0.7}\text{CoCrFeNi}$ HEA after 20 h of oxidation. With an increasing oxidation duration, the Al_2O_3 precipitates formed during 20 h tends to form a discontinuous layer, as observed from the Fig. 15 b. The HEA also displayed a thin sub-layer of metal enriched in oxygen between the external Cr_2O_3 and Al_2O_3 scales. The Fig. 15 b also exhibits the presence of the Al rich layer just beneath Al_2O_3 scales. With further oxidation (200 h) of $\text{Al}_{0.7}\text{CoCrFeNi}$ HEA, the oxidation enriched metal layer eliminated and discontinuous Al_2O_3 oxide scales formed in the previous stage (100 h) became a thick continuous oxide scale. The HEA $\text{Al}_{0.7}\text{CoCrFeNi}$ composed of high enough Al concentration in its composition to promote selective oxidation of Al, which resulted in the generation of a continuous thick Al_2O_3 layer underlying beneath a thin external layer of Cr_2O_3 .

Butler et al [30] proposed that the mechanism for high entropy alloys consisting Ni-Cr-Al elements could be established based on the theory suggested by Giggins-Pettit [39] for Ni-Cr-Al alloys oxidation, Fig. 20. Theory provided oxide maps for the Ni-Cr-Al alloy system. The oxide maps are qualitative in nature, exhibiting the outline of both experimental and empirical observations of the alloy system. Theory segregated the oxide maps into three regions:

- a. Group I correlates to dilute alloys where Al and Cr composition are too short, generate a continuous oxide layer of Al_2O_3 or Cr_2O_3 in the alloy system. Rather, the exterior oxide

scales comprised of $\text{Ni}_2\text{Al}_2\text{O}_4$, NiCr_2O_4 and NiO phases combined with internal oxidation of Al.

- b. Group II belongs to alloy system with high amount of Cr, but with the relatively less Al composition, which results in selective oxidation of chromium, generating an exterior Cr_2O_3 . In this region, an internal oxide subscale of Al_2O_3 layer is formed just beneath the external scale because of internal oxidation of Al. The oxidation procedure in this regime is mostly governed by the diffusional buildup of the outermost Cr_2O_3 oxide layer.
- c. Group III pertains to alloy system consisting of large concentration of Al and Cr, thereby resulting in selective oxidation of Al to generate a thick continuous Al_2O_3 layer with or without Cr_2O_3 oxide layer. The oxidation procedure in this region is dictated by the diffusional formation of a thick Al_2O_3 oxide layer.

In the present investigation, the oxidized $\text{Al}_{0.3}\text{CoCrFeNi}$ HEA formed a thick outer Cr_2O_3 oxide scale along with a discontinuous, interior Al_2O_3 layer, Fig. 14. The oxidized $\text{Al}_{0.3}\text{CoCrFeNi}$ HEA displayed microstructures that resemble Group II alloys. The long-term oxidation performance of HEAs much relies upon Al and/or Cr contents on its subsurface along with extent of elemental dispersion caused due to oxide scale formation. As observed from Fig. 14, EDS on the cross-section of $\text{Al}_{0.3}\text{CoCrFeNi}$ sample oxidized at 1100°C for 200 h, exhibited an Al and Cr depletion layer just beneath the internal Al_2O_3 . Rise in the depletion layer lowers the ability of HEA to reform a protective oxide scale. In consequence, the depleted region may develop lower protective oxide scales in the presence of oxygen environment. On the basis of microstructural analysis, the oxidized $\text{Al}_{0.7}\text{CoCrFeNi}$ HEA is inconsistent with Group III alloy. It's because of the formation of a thin external Cr_2O_3 oxide scale with an underlying very thick continuous Al_2O_3 layer. The EDS of oxidized $\text{Al}_{0.7}\text{CoCrFeNi}$ HEA just beneath the Al_2O_3 layer, Fig. 15 displays presence of Al approximately 6 at. % all across the cross-section morphology,

indicating absence of the Al depletion layer which was observed in case of oxidized Al_{0.3}CoCrFeNi HEA. The amount of the Al present below the oxide scale is well within the limit to yield appropriate oxidation resistance in HEA.

An examination of the mass changes (Fig. 10), demonstrated that the oxidation of Al_{0.3}CoCrFeNi and Al_{0.7}CoCrFeNi HEAs occurred initially via transient stage followed by parabolic stages. During the transient stage of oxidation, nuclei of various oxides (mostly NiO and spinels) formed, which lead to development of thin layer of oxide scales all over the surface of both HEAs. Once these oxide scales become continuous, diffusion within the alloy resulted in the emergence of a sub-scale below the transient oxide scales comprising of Al₂O₃ and Cr₂O₃ oxide layer. This is followed by a transformation from transient stage to parabolic stage. Ultimately, at this stage growth of protective Al₂O₃ and Cr₂O₃ oxide scales occurred. The further state (thickness and position) of these oxide scales mostly dependent on the alloy composition. This behaviour of both Al_{0.3}CoCrFeNi and Al_{0.7}CoCrFeNi HEAs is in consistence with some of the other well-examined oxidation behaviour of model Co-Cr-Al, Fe-Cr-Al and Ni-Cr-Al alloy systems [36]. The parabolic rate constant (K_p) value for the HEA Al_{0.3}CoCrFeNi and Al_{0.7}CoCrFeNi was found to be 1.7×10^{-12} and 3.8×10^{-13} respectively. The K_p for both HEAs in this study were observed to be within the domain of 10^{-11} - 10^{-13} , which is similar to the values determined for Group II and Group III Ni-Cr-Al alloys [37].

The prevailing tendency of rise in Al content and decreased mass changes in HEA considered in present study corresponds to the formation of Al₂O₃ sub-scale. It was observed that both HEAs investigated in present work formed an exterior Cr₂O₃ oxide layer. However, high Al content led to the formation of thin outer Cr₂O₃ oxide layer and may further generate a thick continuous underlying Al₂O₃ sub-scale. It is presumed that the above aspect increases the oxidation resistance in high Al content alloys.

5. Conclusions

It is concluded that direct laser deposition is a versatile method in order to manufacture high entropy alloys with additive manufacturing process. Two $\text{Al}_x\text{CoCrFeNi}$ HEA with different Al content ($x=0.3$ and 0.7) were fabricated using the additive manufacturing technique. The microstructure and mechanical properties of the direct laser deposited samples were compared. Oxidation study of additive manufactured samples was carried out in a static atmosphere at temperature 1100°C . Microstructural characterization of both oxidized HEAs was investigated. The results can be summarized as follows:

- a. The FCC $\text{Al}_{0.3}\text{CoCrFeNi}$ HEA exhibited a coarse columnar structure, whereas the FCC+BCC HEA ($\text{Al}_{0.7}\text{CoCrFeNi}$) showed a coarse dendritic grain structure. This change in crystal structure was a result of increase in aluminum concentration.
- b. The increased Al content resulted in increased microhardness. The average microhardness of $\text{Al}_{0.3}\text{CoCrFeNi}$ was observed to be around 170HV, whereas for $\text{Al}_{0.7}\text{CoCrFeNi}$ it was found to be around 380HV.
- c. The oxidation rate for both HEAs increased with duration and showed a parabolic growth after an initial transient stage. The mass gain for HEA $\text{Al}_{0.3}\text{CoCrFeNi}$ was higher as compared to $\text{Al}_{0.7}\text{CoCrFeNi}$ during the entire duration.
- d. The parabolic rate constant (K_p) value for the HEA $\text{Al}_{0.3}\text{CoCrFeNi}$ and $\text{Al}_{0.7}\text{CoCrFeNi}$ was found to be 1.7×10^{-12} and 3.8×10^{-13} respectively. The K_p value for both HEAs was observed to be within the domain of 10^{-11} - 10^{-13} , which were comparable to those of Ni-Cr-Al alloys.
- e. Cyclic oxidation of the HEAs at temperature 1100°C in the static atmosphere promoted the formation of Cr_2O_3 , Al_2O_3 , NiO and NiCr_2O_4 oxides on the oxidized surface of HEAs.

- f. For low content Al HEA i.e. $\text{Al}_{0.3}\text{CoCrFeNi}$, an exterior, thick oxide layer of Cr_2O_3 formed along with discontinuous Al_2O_3 sub-scale in the form of coarse precipitate. Cross-section morphology of $\text{Al}_{0.3}\text{CoCrFeNi}$ sample oxidized at 1100°C for 200 h, showed an Al and Cr depletion layer just beneath the internal Al_2O_3 scale. Rise in the depletion layer lowers the ability of HEA to reform a protective oxide scale.
- g. With the increase in Al content ($\text{Al}_{0.7}\text{CoCrFeNi}$), the thickness of Cr_2O_3 oxide scale was reduced for oxidized HEAs. As expected, the $\text{Al}_{0.7}\text{CoCrFeNi}$ HEAs developed a continuous Al_2O_3 scale, whose thickness increased with longer oxidation duration, thereby enhancing its oxidation resistance.

References

- [1] Cantor, Brain, I. T. H. Chang, P. Knight, and A. J. B. Vincent. "Microstructural development in equiatomic multicomponent alloys." *Materials Science and Engineering: A* 375 (2004): 213-218.
- [2] Zhang, Yong, Ting Ting Zuo, Zhi Tang, Michael C. Gao, Karin A. Dahmen, Peter K. Liaw, and Zhao Ping Lu. "Microstructures and properties of high-entropy alloys." *Progress in Materials Science* 61 (2014): 1-93.
- [3] Vaidya, Mayur, Garlapati Mohan Muralikrishna, and Budaraju Srinivasa Murty. "High-entropy alloys by mechanical alloying: A review." *Journal of Materials Research* 34, no. 5 (2019): 664-686.
- [4] Ye, Y. F., Q. Wang, J. Lu, C. T. Liu, and Y. Yang. "High-entropy alloy: challenges and prospects." *Materials Today* 19, no. 6 (2016): 349-362.

- [5] Yang, X., and Yong Zhang. "Prediction of high-entropy stabilized solid-solution in multi-component alloys." *Materials Chemistry and Physics* 132, no. 2-3 (2012): 233-238.
- [6] Sheng, G. U. O., and Chain Tsuan Liu. "Phase stability in high entropy alloys: formation of solid-solution phase or amorphous phase." *Progress in Natural Science: Materials International* 21, no. 6 (2011): 433-446.
- [7] Guo, Sheng, Chun Ng, Jian Lu, and C. T. Liu. "Effect of valence electron concentration on stability of fcc or bcc phase in high entropy alloys." *Journal of applied physics* 109, no. 10 (2011): 103505.
- [8] Li, C., J. C. Li, M. Zhao, and Q. Jiang. "Effect of aluminum contents on microstructure and properties of $\text{Al}_x\text{CoCrFeNi}$ alloys." *Journal of Alloys and Compounds* 504 (2010): S515-S518.
- [9] Wu, Jien-Min, Su-Jien Lin, Jien-Wei Yeh, Swe-Kai Chen, Yuan-Sheng Huang, and Hung-Cheng Chen. "Adhesive wear behavior of $\text{Al}_x\text{CoCrCuFeNi}$ high-entropy alloys as a function of aluminum content." *Wear* 261, no. 5-6 (2006): 513-519.
- [10] Lee, C. P., C. C. Chang, Y. Y. Chen, J. W. Yeh, and H. C. Shih. "Effect of the aluminium content of $\text{Al}_x\text{CrFe}_{1.5}\text{MnNi}_{0.5}$ high-entropy alloys on the corrosion behaviour in aqueous environments." *Corrosion Science* 50, no. 7 (2008): 2053-2060.
- [11] Wang, Woei-Ren, Wei-Lin Wang, and Jien-Wei Yeh. "Phases, microstructure and mechanical properties of $\text{Al}_x\text{CoCrFeNi}$ high-entropy alloys at elevated temperatures." *Journal of Alloys and Compounds* 589 (2014): 143-152.
- [12] Kao, Yih-Farn, Ting-Jie Chen, Swe-Kai Chen, and Jien-Wei Yeh. "Microstructure and mechanical property of as-cast,-homogenized, and-deformed $\text{Al}_x\text{CoCrFeNi}$ ($0 \leq x \leq 2$) high-entropy alloys." *Journal of Alloys and Compounds* 488, no. 1 (2009): 57-64.

- [13] Wang, Woei-Ren, Wei-Lin Wang, Shang-Chih Wang, Yi-Chia Tsai, Chun-Hui Lai, and Jien-Wei Yeh. "Effects of Al addition on the microstructure and mechanical property of $\text{Al}_x\text{CoCrFeNi}$ high-entropy alloys." *Intermetallics* 26 (2012): 44-51.
- [14] Praveen, S., B. S. Murty, and Ravi S. Kottada. "Alloying behavior in multi-component AlCoCrCuFe and NiCoCrCuFe high entropy alloys." *Materials Science and Engineering: A534* (2012): 83-89.
- [15] Fang, Sicong, Weiping Chen, and Zhiqiang Fu. "Microstructure and mechanical properties of twinned $\text{Al}_{0.5}\text{CrFeNiCo}_{0.3}\text{Cu}_{0.2}$ high entropy alloy processed by mechanical alloying and spark plasma sintering." *Materials & Design* (1980-2015) 54 (2014): 973-979.
- [16] Ji, Wei, Zhengyi Fu, Weimin Wang, Hao Wang, Jinyong Zhang, Yucheng Wang, and Fan Zhang. "Mechanical alloying synthesis and spark plasma sintering consolidation of CoCrFeNiAl high-entropy alloy." *Journal of Alloys and Compounds* 589 (2014): 61-66.
- [17] Brif, Yevgeni, Meurig Thomas, and Iain Todd. "The use of high-entropy alloys in additive manufacturing." *Scripta Materialia* 99 (2015): 93-96.
- [18] Lin, Y. C., and Y. H. Cho. "Elucidating the microstructural and tribological characteristics of NiCrAlCoCu and NiCrAlCoMo multicomponent alloy clad layers synthesized in situ." *Surface and Coatings Technology* 203, no. 12 (2009): 1694-1701.
- [19] Huo, Wen-yi, Hai-fang Shi, Xin Ren, and Jing-yuan Zhang. "Microstructure and wear behavior of CoCrFeMnNbNi high-entropy alloy coating by TIG cladding." *Advances in Materials Science and Engineering* 2015 (2015).
- [20] Wang, Rui, Kai Zhang, Christopher Davies, and Xinhua Wu. "Evolution of microstructure, mechanical and corrosion properties of AlCoCrFeNi high-entropy alloy

prepared by direct laser fabrication." *Journal of Alloys and Compounds* 694 (2017): 971-981.

- [21] Li, Mu, Jaume Gazquez, Albina Borisevich, Rohan Mishra, and Katharine M. Flores. "Evaluation of microstructure and mechanical property variations in Al_xCoCrFeNi high entropy alloys produced by a high-throughput laser deposition method." *Intermetallics* 95 (2018): 110-118.
- [22] Joseph, Jithin, Tom Jarvis, Xinhua Wu, Nicole Stanford, Peter Hodgson, and Daniel Mark Fabijanic. "Comparative study of the microstructures and mechanical properties of direct laser fabricated and arc-melted Al_xCoCrFeNi high entropy alloys." *Materials Science and Engineering: A* 633 (2015): 184-193.
- [23] Chao, Qi, Tingting Guo, Tom Jarvis, Xinhua Wu, Peter Hodgson, and Daniel Fabijanic. "Direct laser deposition cladding of Al_xCoCrFeNi high entropy alloys on a high-temperature stainless steel." *Surface and Coatings Technology* 332 (2017): 440-451.
- [24] Kunce, I., M. Polanski, K. Karczewski, T. Plocinski, and K. J. Kurzydowski. "Microstructural characterisation of high-entropy alloy AlCoCrFeNi fabricated by laser engineered net shaping." *Journal of Alloys and Compounds* 648 (2015): 751-758.
- [25] Ocelik, V., N. Janssen, S. N. Smith, and J. Th M. De Hosson. "Additive manufacturing of high-entropy alloys by laser processing." *JOM* 68, no. 7 (2016): 1810-1818.
- [26] Ang, Andrew Siao Ming, Christopher C. Berndt, Mitchell L. Sesso, Ameer Anupam, S. Praveen, Ravi Sankar Kottada, and B. S. Murty. "Plasma-sprayed high entropy alloys: Microstructure and properties of AlCoCrFeNi and MnCoCrFeNi." *Metallurgical and Materials Transactions A* 46, no. 2 (2015): 791-800.
- [27] Juliusz Dębrowa, Grzegorz Cieslak, Mirosław Stygar, Krzysztof Mroczka, Katarzyna Berent, Tadeusz Kulik, Marek Danielewski, Influence of Cu content on high

temperature oxidation behavior of AlCoCrCu_xFeNi high entropy alloys (x = 0; 0.5; 1), *Intermetallics* 84 52-61(2017).

- [28] Todd M. Butler, Mark L. Weaver, Oxidation behavior of arc melted AlCoCrFeNi multi-component high-entropy alloys, *Journal of Alloys and Compounds* 674 229-244 (2016).
- [29] Gang Zhua, Ying Liua,b, Jinwen Yea, Early high-temperature oxidation behavior of Ti(C,N)-based cermets with multi-component AlCoCrFeNi high-entropy alloy binder, *Int. Journal of Refractory Metals and Hard Materials* 44,35–41(2014).
- [30] Butler, T. M., J. P. Alfano, R. L. Martens, and M. L. Weaver. "High-temperature oxidation behavior of Al-Co-Cr-Ni-(Fe or Si) multicomponent high-entropy alloys." *Jom* 67, no. 1 (2015): 246-259.
- [31] Zhou, Y. J., Y. Zhang, F. J. Wang, and G. L. Chen. "Phase transformation induced by lattice distortion in multiprincipal component Co Cr Fe Ni Cu x Al 1– x solid-solution alloys." *Applied Physics Letters* 92, no. 24 (2008): 241917.
- [32] Zhang, Hui, Ye Pan, Yizhu He, and Huisheng Jiao. "Microstructure and properties of 6FeNiCoSiCrAlTi high-entropy alloy coating prepared by laser cladding." *Applied Surface Science* 257, no. 6 (2011): 2259-2263.
- [33] Yue, T. M., H. Xie, X. Lin, H. O. Yang, and G. H. Meng. "Solidification behaviour in laser cladding of AlCoCrCuFeNi high-entropy alloy on magnesium substrates." *Journal of alloys and compounds* 587 (2014): 588-593.
- [34] Takeuchi, Akira, and Akihisa Inoue. "Classification of bulk metallic glasses by atomic size difference, heat of mixing and period of constituent elements and its application to characterization of the main alloying element." *Materials Transactions* 46, no. 12 (2005): 2817-2829.

- [35] Takeuchi, Akira, and Akihisa Inoue. "Calculations of mixing enthalpy and mismatch entropy for ternary amorphous alloys." *Materials transactions, JIM* 41, no. 11 (2000): 1372-1378.
- [36] Birks, Neil, Gerald H. Meier, and Frederick S. Pettit. *Introduction to the high temperature oxidation of metals*. Cambridge University Press, 2006.
- [37] Young, David John. *High temperature oxidation and corrosion of metals*. Vol. 1. Elsevier, 2008.
- [38] Yeh, Jien Wei, Yu Liang Chen, Su Jien Lin, and Swe Kai Chen. "High-entropy alloys—a new era of exploitation." In *Materials Science Forum*, vol. 560, pp. 1-9. Trans Tech Publications, 2007.
- [39] Giggins, C. S., and FSt Pettit. "Oxidation of Ni-Cr-Al Alloys between 1000 and 1200 C." *Journal of the Electrochemical Society* 118, no. 11 (1971): 1782-1790.

Table 1 The values of the parabolic constants for various HEAs

ALLOY	K_p ($\text{g}^2\text{cm}^{-4}\text{s}^{-1}$)	TEMPERATURE	REFERENCE
$\text{Al}_{0.3}\text{CoCrFeNi}$	1.7×10^{-12}	1100 °C	Present Work
$\text{Al}_{0.7}\text{CoCrFeNi}$	3.8×10^{-13}		
$\text{Al}_8(\text{NiCrCoFe})_{92}$	2.5×10^{-12}	1050 °C	[28]
$\text{Al}_{10}(\text{NiCrCoFe})_{90}$	1.8×10^{-12}		
$\text{Al}_{12}(\text{NiCrCoFe})_{88}$	4.6×10^{-13}		
$\text{Al}_{15}(\text{NiCrCoFe})_{85}$	4.6×10^{-12}		
$\text{Al}_{10}\text{Cr}_{22.5}\text{Co}_{22.5}\text{Ni}_{22.5}\text{Fe}_{22.5}$	1.1×10^{-11}	1050 °C	[30]
$\text{Al}_{20}\text{Cr}_{25}\text{Co}_{25}\text{Ni}_{25}\text{Si}_5$	5.1×10^{-15}		
$\text{Al}_{15}\text{Cr}_{10}\text{Co}_{35}\text{Ni}_{35}\text{Si}_5$	3.6×10^{-12}		

Fig 1: SEM images of powder mixtures with corresponding EDS (a) $\text{Al}_{0.3}\text{CoCrFeNi}$ and (b) $\text{Al}_{0.7}\text{CoCrFeNi}$.

Fig 2: XRD patterns of HEAs (a) $\text{Al}_{0.3}\text{CoCrFeNi}$ (b) $\text{Al}_{0.7}\text{CoCrFeNi}$.

Fig 3: BSE images of (a) $\text{Al}_{0.3}\text{CoCrFeNi}$ (b) $\text{Al}_{0.7}\text{CoCrFeNi}$.

Fig 4: Elemental Compositions at 7 different places on HEA $\text{Al}_{0.3}\text{CoCrFeNi}$

Fig 5: Elemental Compositions at 7 different places on HEA $\text{Al}_{0.7}\text{CoCrFeNi}$

Fig 6: Element maps of the HEA alloy $\text{Al}_{0.3}\text{CoCrFeNi}$.

Fig 7: Element maps of the HEA alloy $\text{Al}_{0.7}\text{CoCrFeNi}$.

Fig 8: EBSD analysis of two high entropy alloys (a) $\text{Al}_{0.3}\text{CoCrFeNi}$ (b) $\text{Al}_{0.7}\text{CoCrFeNi}$.

Fig 9: Hardness plots along the two sections of the two HEAs (a) $\text{Al}_{0.3}\text{CoCrFeNi}$ (b) $\text{Al}_{0.7}\text{CoCrFeNi}$.

Fig 10: Mass change patterns of the two HEAs $\text{Al}_{0.3}\text{CoCrFeNi}$ and $\text{Al}_{0.7}\text{CoCrFeNi}$ (a) normal plot and (b) parabolic plot.

Fig. 11: TGA for two HEAs $\text{Al}_{0.3}\text{CoCrFeNi}$ and $\text{Al}_{0.7}\text{CoCrFeNi}$

Fig. 12: SEM micrographs of the oxide scale morphology developed on $\text{Al}_{0.3}\text{CoCrFeNi}$ at 1100°C for (a) 20 h (b) 100 h and (c) 200 h with corresponding EDS.

Fig. 13: SEM micrographs of the oxide scale morphology developed on $\text{Al}_{0.7}\text{CoCrFeNi}$ at 1100°C for (a) 20 h (b) 100 h and (c) 200 h with corresponding EDS.

Fig. 14: Cross-sectional SEM micrographs of the oxide scale morphology developed on $\text{Al}_{0.3}\text{CoCrFeNi}$ at 1100°C after (a) 20 h (b) 100 h and (c) 200 h with corresponding EDS.

Fig. 15: Cross-sectional SEM micrographs of the oxide scale morphology developed on $\text{Al}_{0.7}\text{CoCrFeNi}$ at 1100°C after (a) 20 h (b) 100 h and (c) 200 h with corresponding EDS.

Fig. 16: XRD patterns of surface on oxidized HEAs (a) $\text{Al}_{0.3}\text{CoCrFeNi}$ for 20 h (b) $\text{Al}_{0.3}\text{CoCrFeNi}$ for 200 h (c) $\text{Al}_{0.7}\text{CoCrFeNi}$ for 20 h and (d) $\text{Al}_{0.7}\text{CoCrFeNi}$ for 200 h.

Fig. 17: Correlation of various phases with respect to valence electron concentration.

Fig. 18: (a) Line scan (b) corresponding selected area EDS of the surface oxide scale morphology developed on $\text{Al}_{0.3}\text{CoCrFeNi}$ at 1100°C for 20 h.

Fig. 19: (a) Line scan (b) corresponding selected area EDS of the surface oxide scale morphology developed on $\text{Al}_{0.7}\text{CoCrFeNi}$ at 1100°C for 20 h.

Fig. 20: Schematic diagram showing the oxidation mechanisms of the Ni-Cr-Al based on Giggins-Petit theory [39].

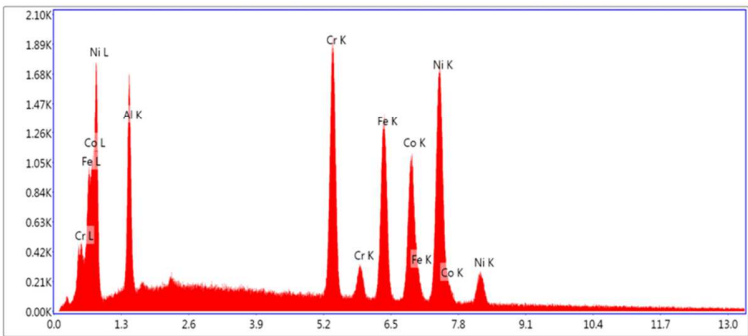
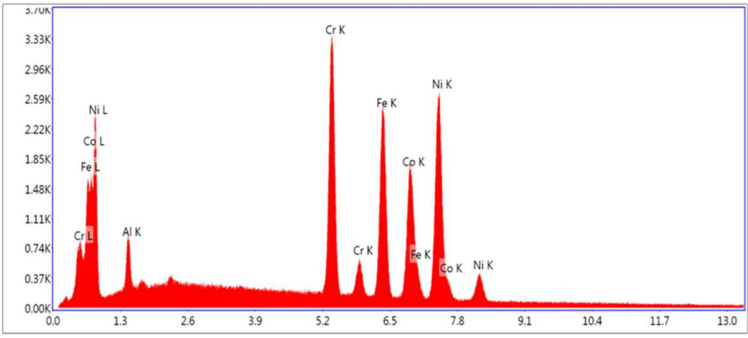


Fig. 1.

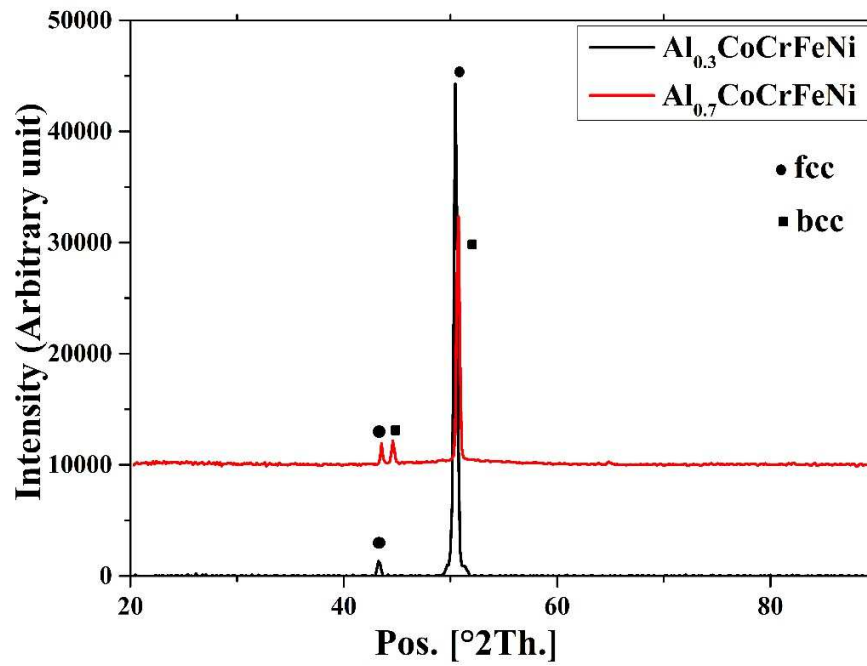


Fig. 2.

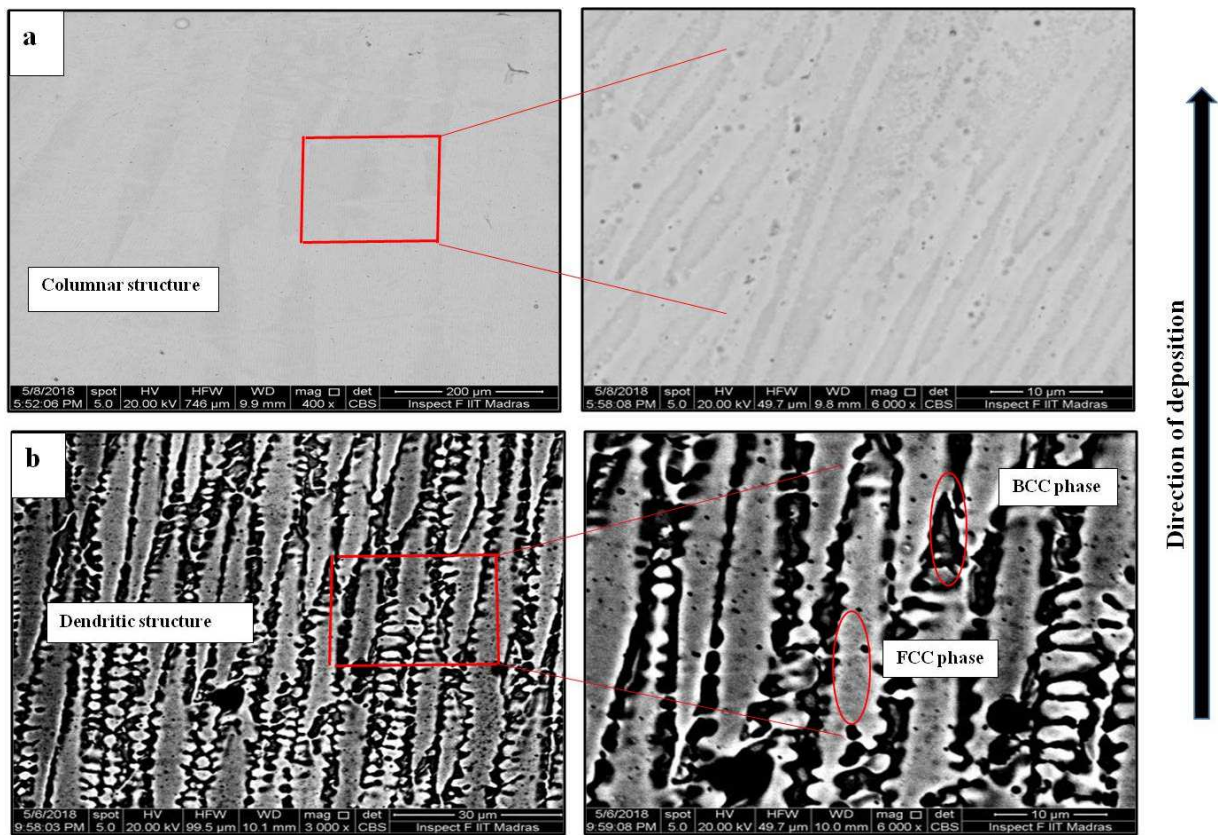
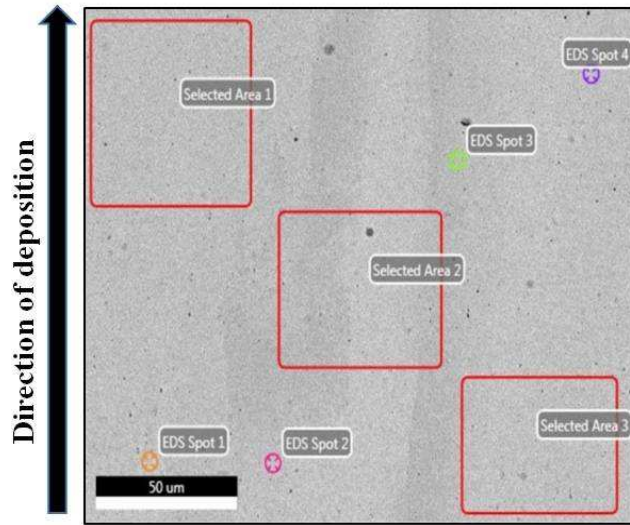
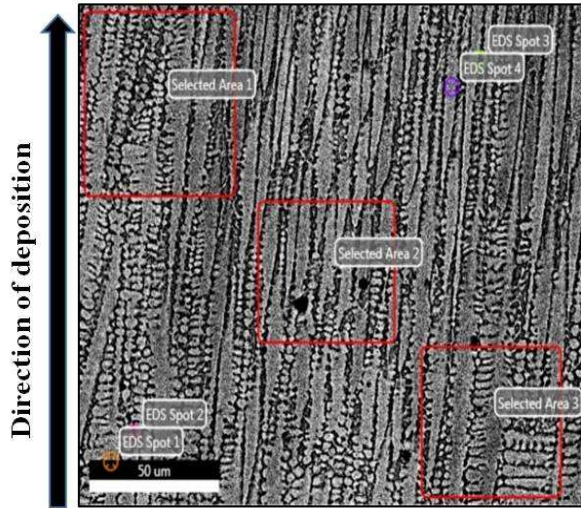


Fig. 3.



Element	Ideal At. %	Average At.% (a)
Al	7	6.5
Cr	23	20.15
Fe	23	20.51
Co	23	19.19
Ni	23	33.53

Fig. 4.



Element	Ideal At. %	Average At.% (a)	Spot 3 of Region 1	Spot 4 of Region 1
Al	14	15.04	19.16	13.78
Cr	21.5	17.3	15.66	17.12
Fe	21.5	24.44	23.38	26.43
Co	21.5	15.42	13.90	15.66
Ni	21.5	27.77	27.70	26.06

Fig. 5.

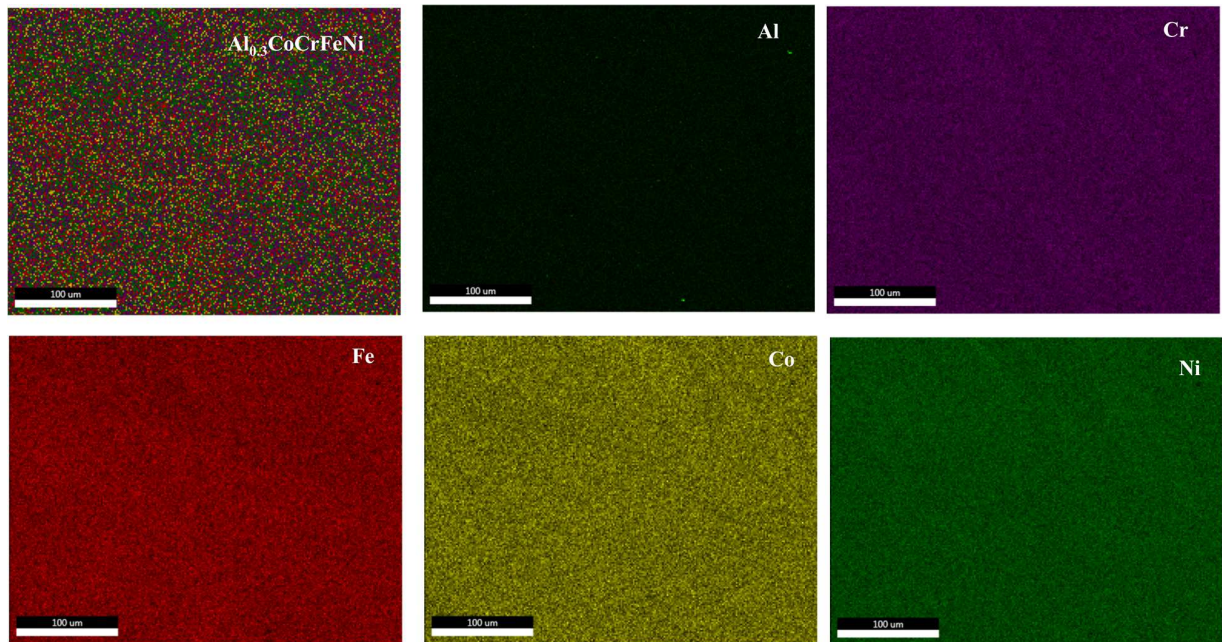


Fig. 6.

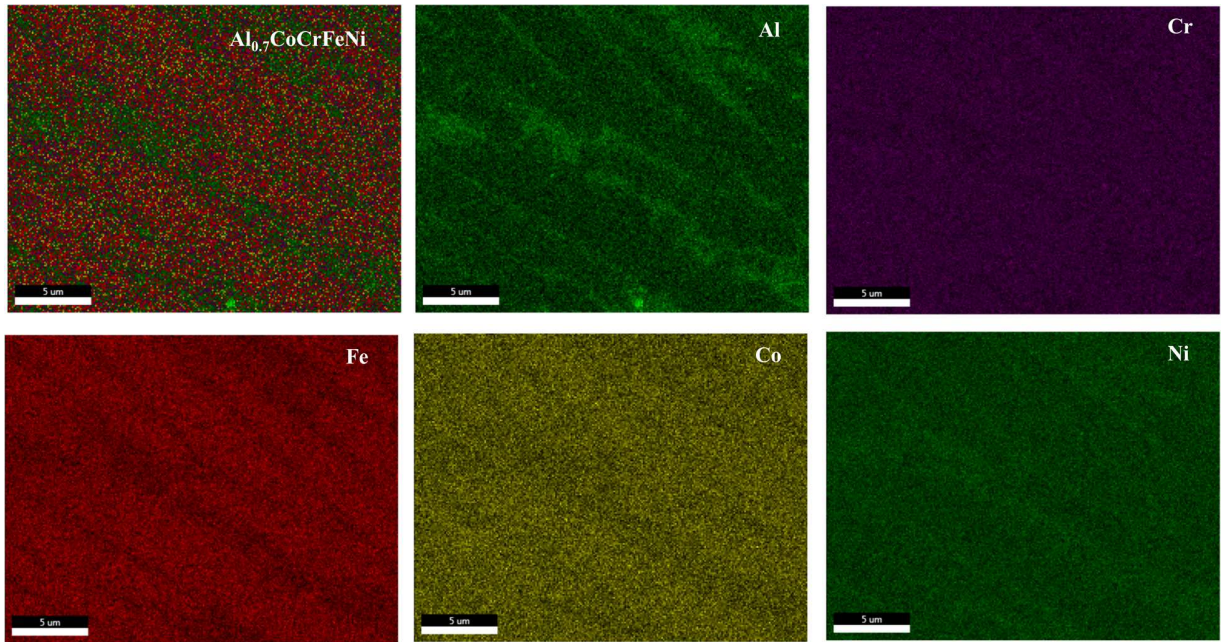


Fig. 7.

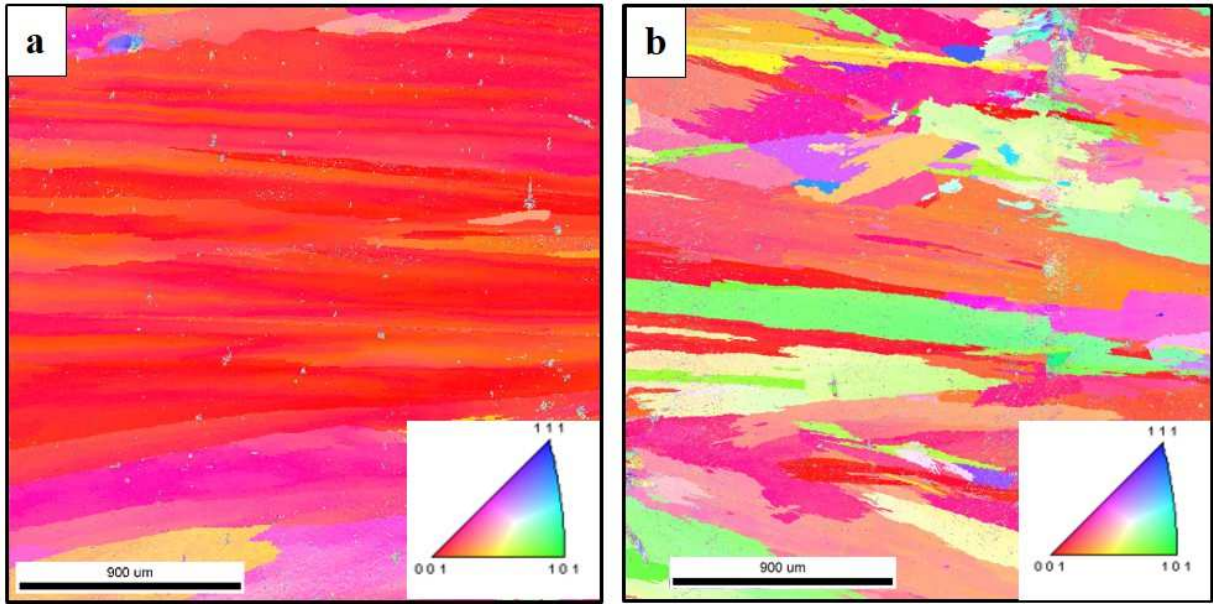


Fig. 8.

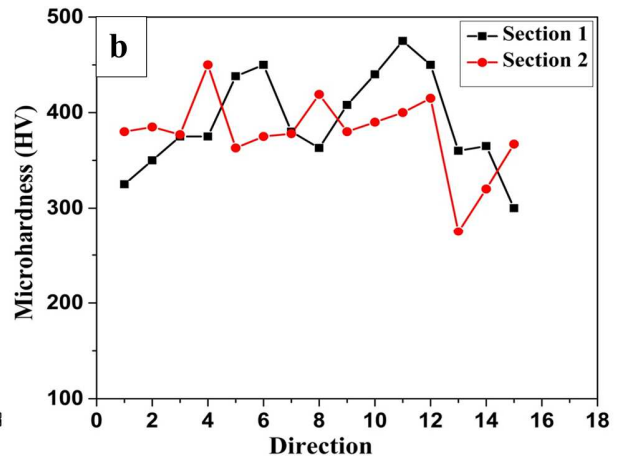
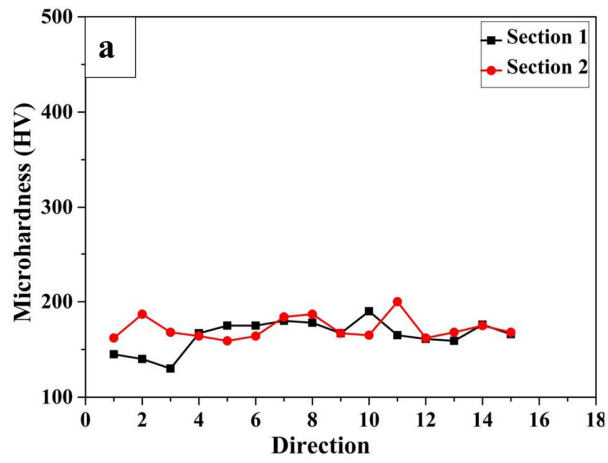


Fig. 9.

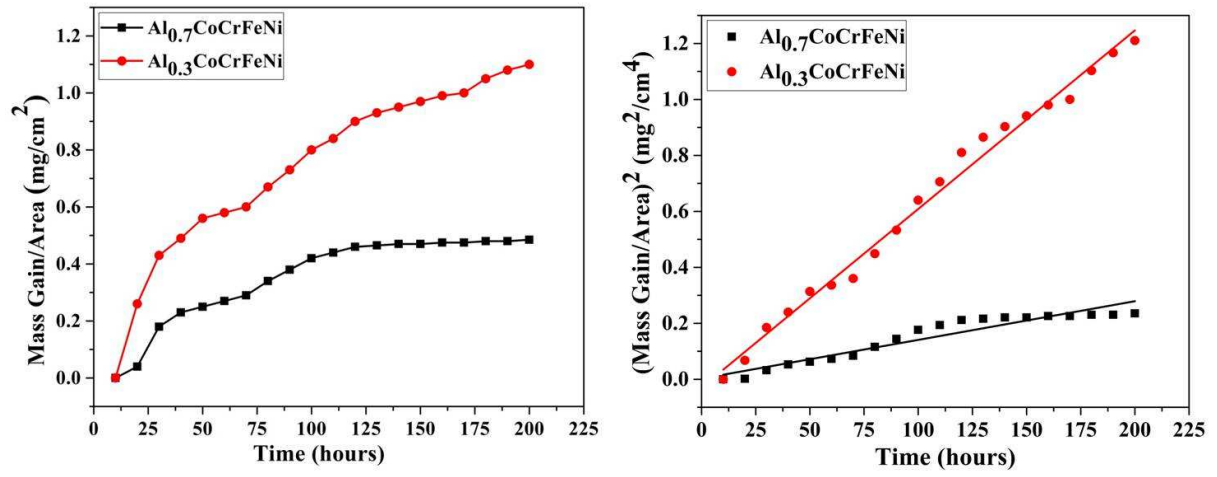


Fig. 10.

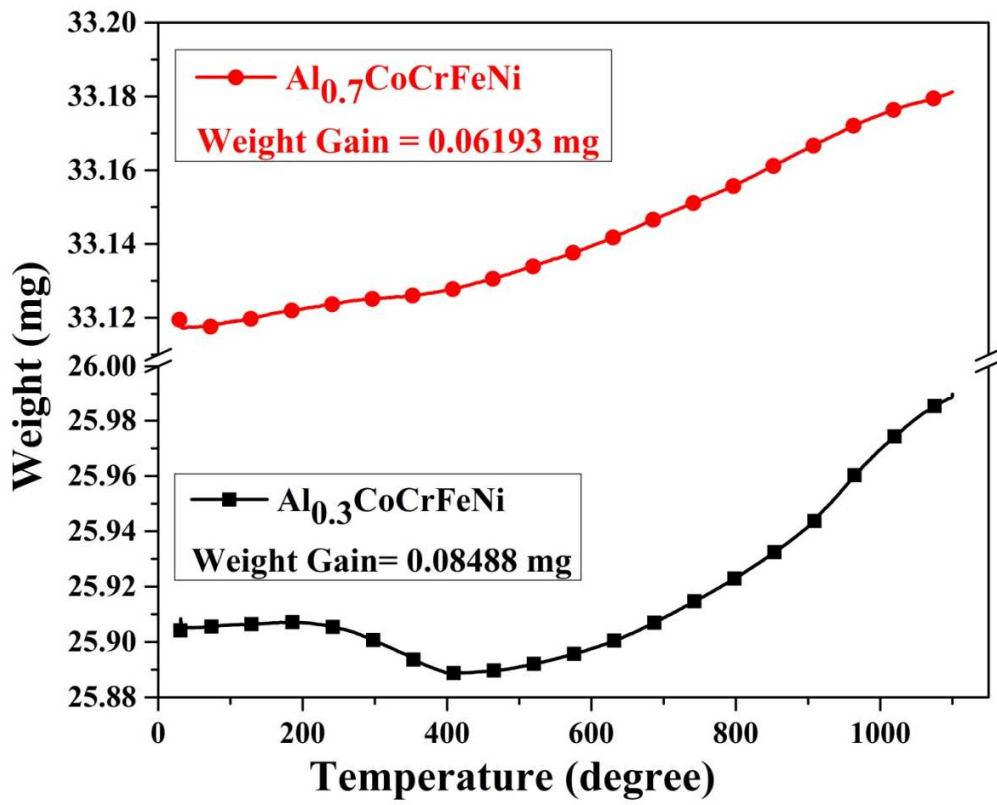
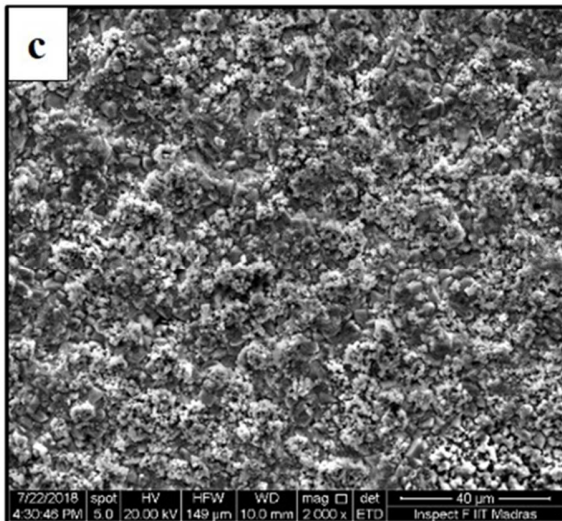
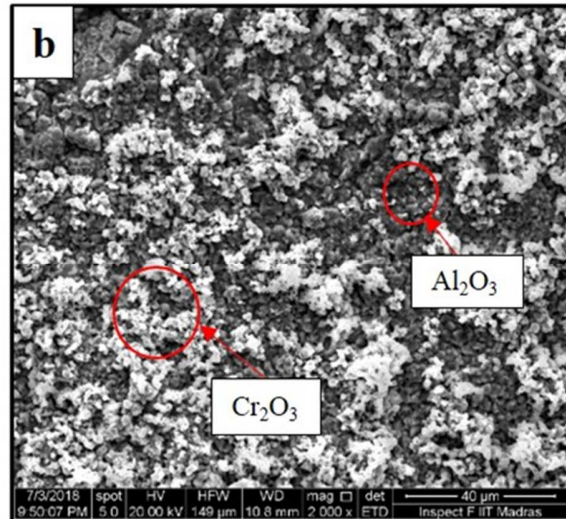
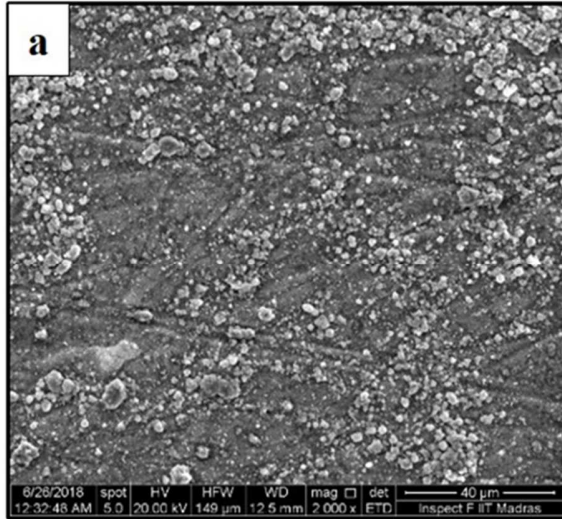


Fig. 11.



Element	Atomic % (a)	Atomic % (b)	Atomic % (c)
O K	46.84	38.07	32.99
AlK	17.97	2.58	1.38
CrK	17.51	52.20	54.03
FeK	5.67	2.39	3.20
CoK	4.61	1.83	3.04
NiK	7.40	2.93	5.36

Fig. 12.

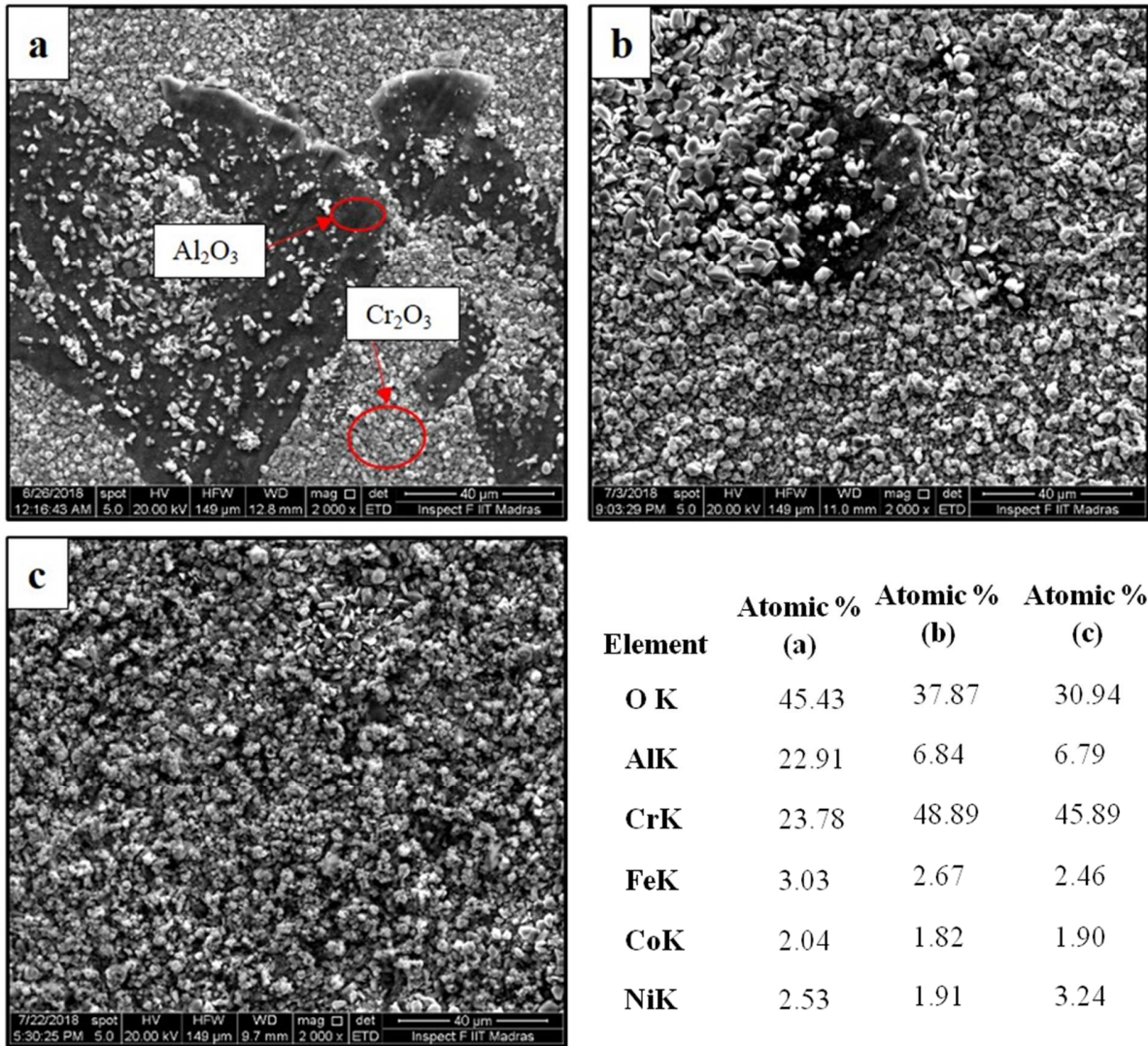


Fig. 13.

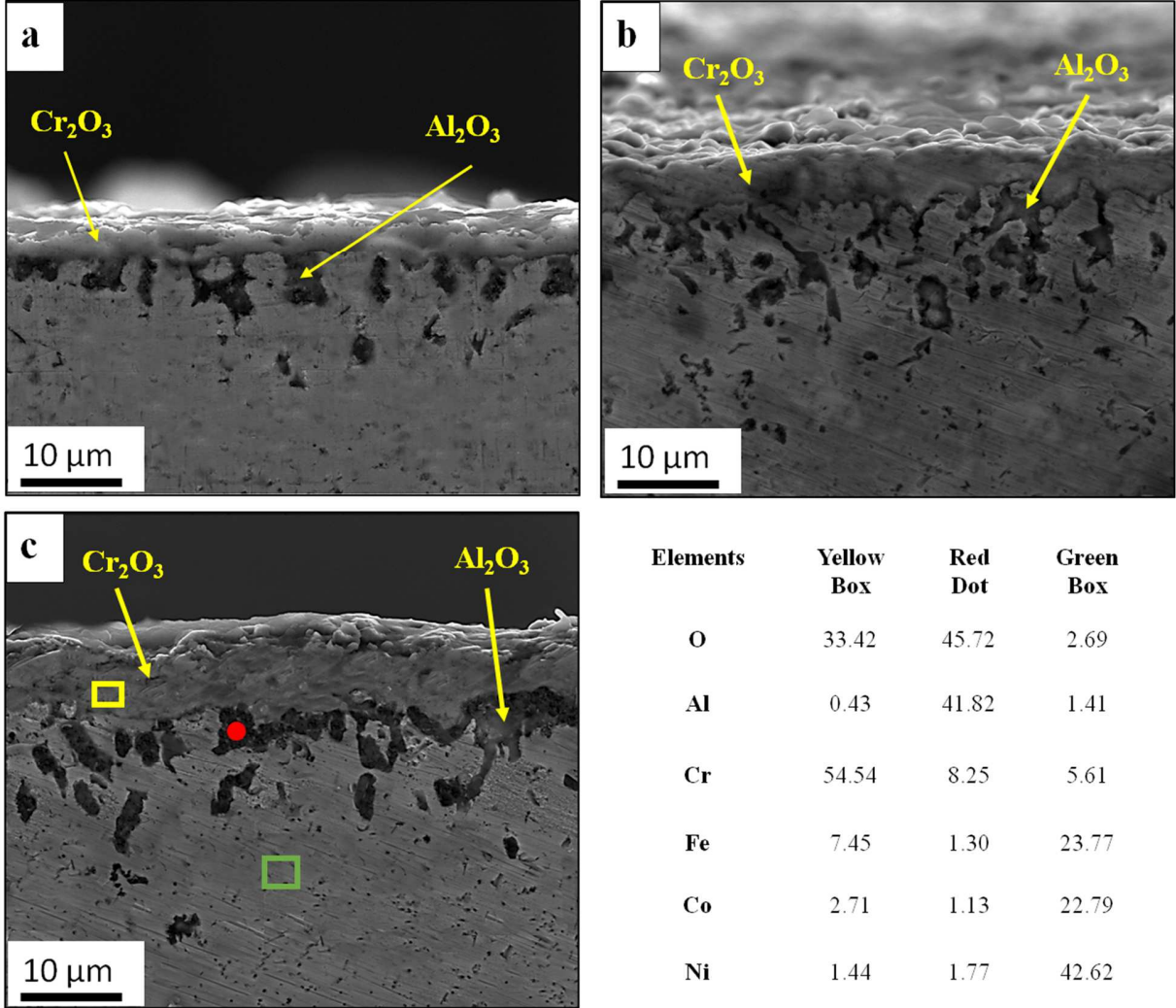


Fig. 14.

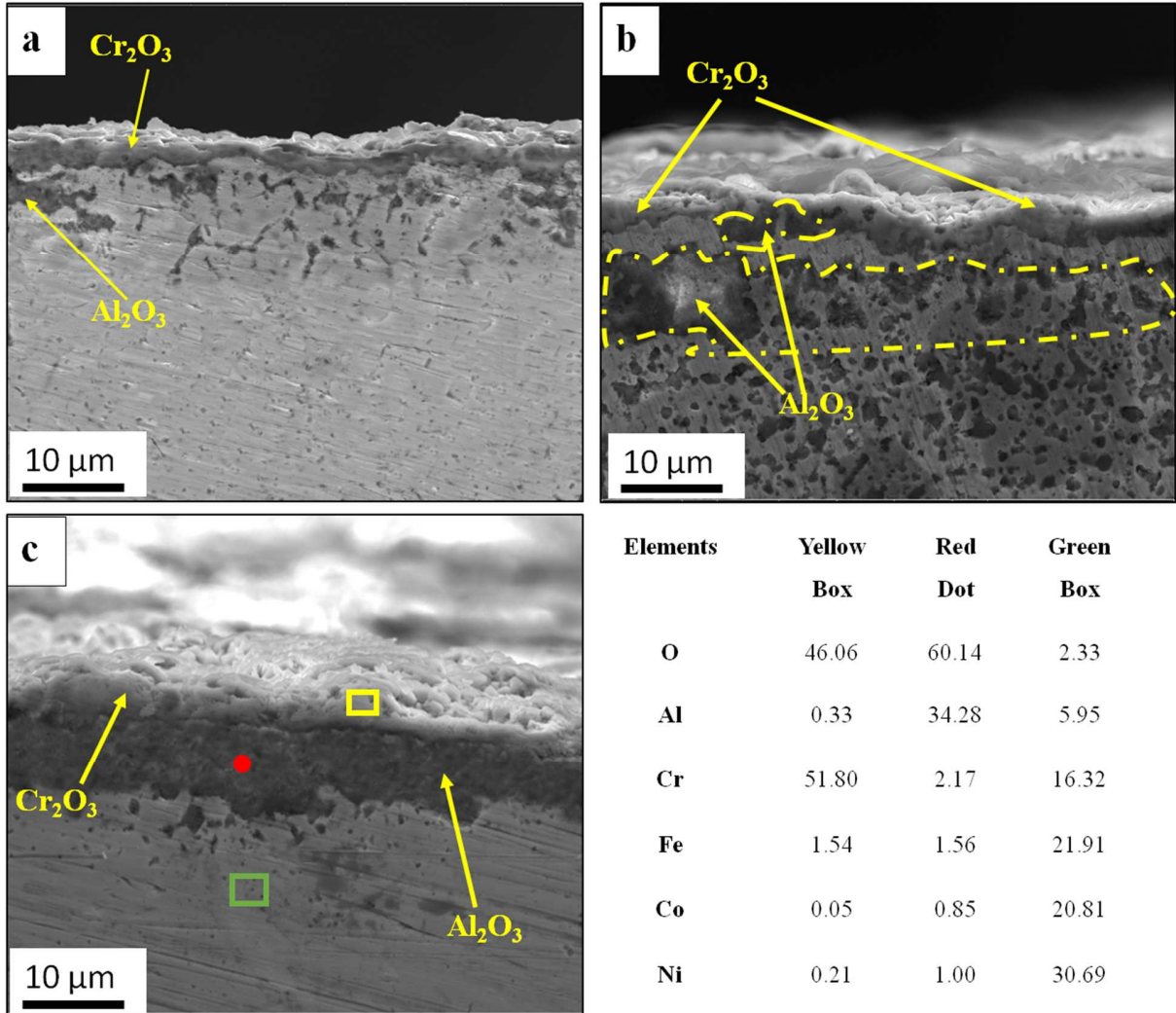


Fig. 15.

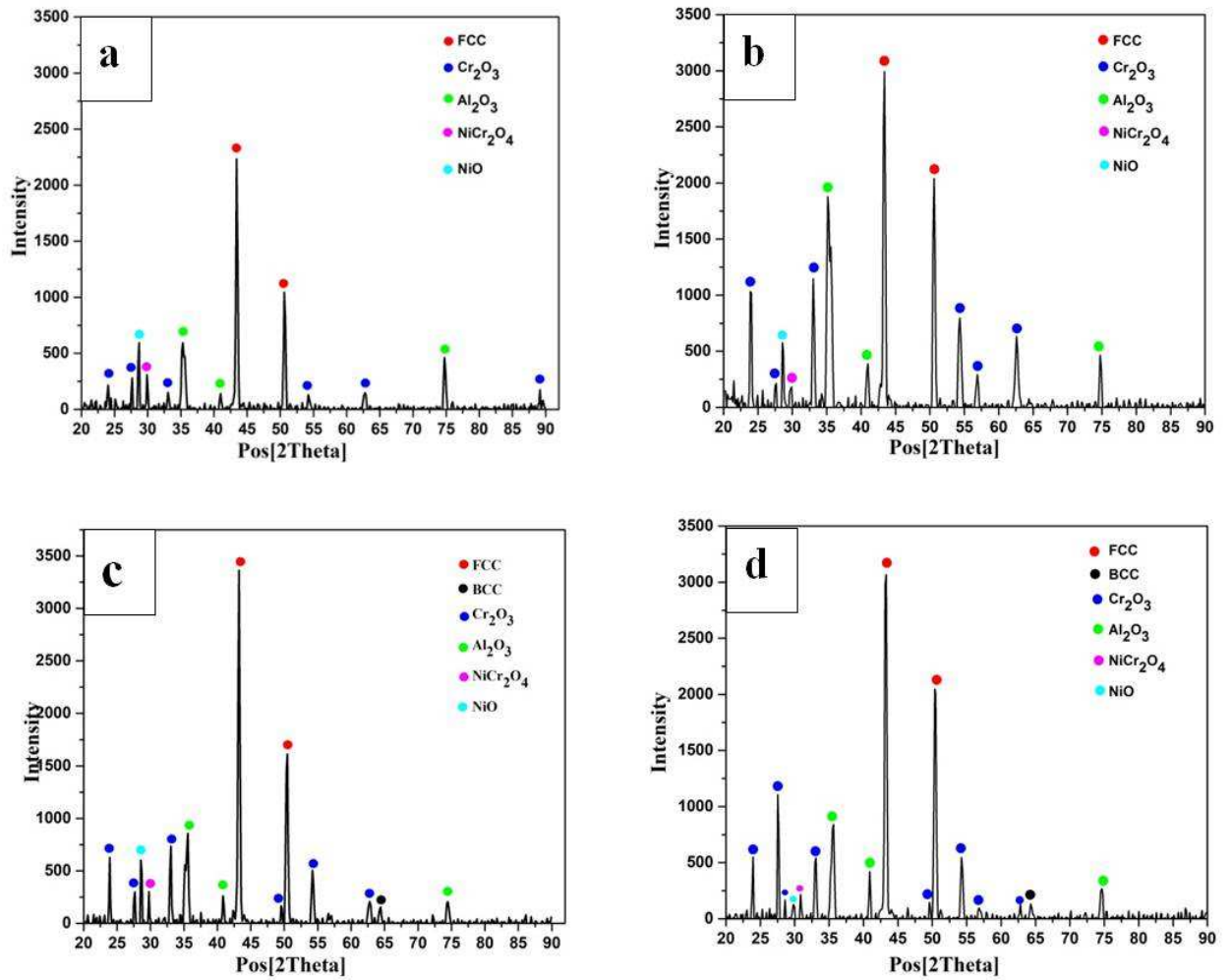


Fig. 16.

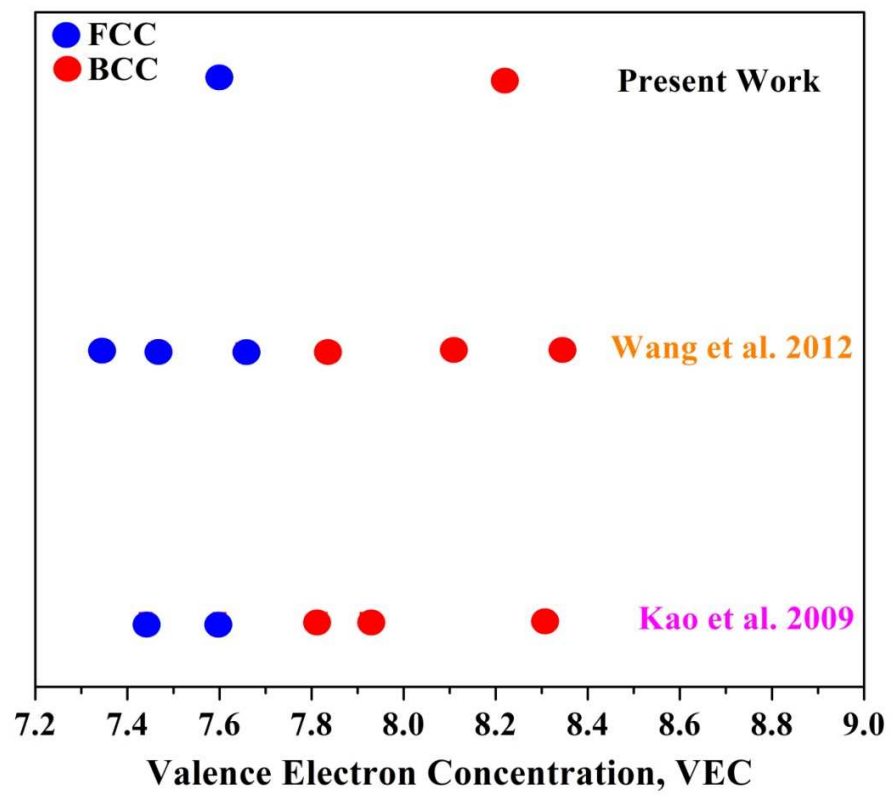
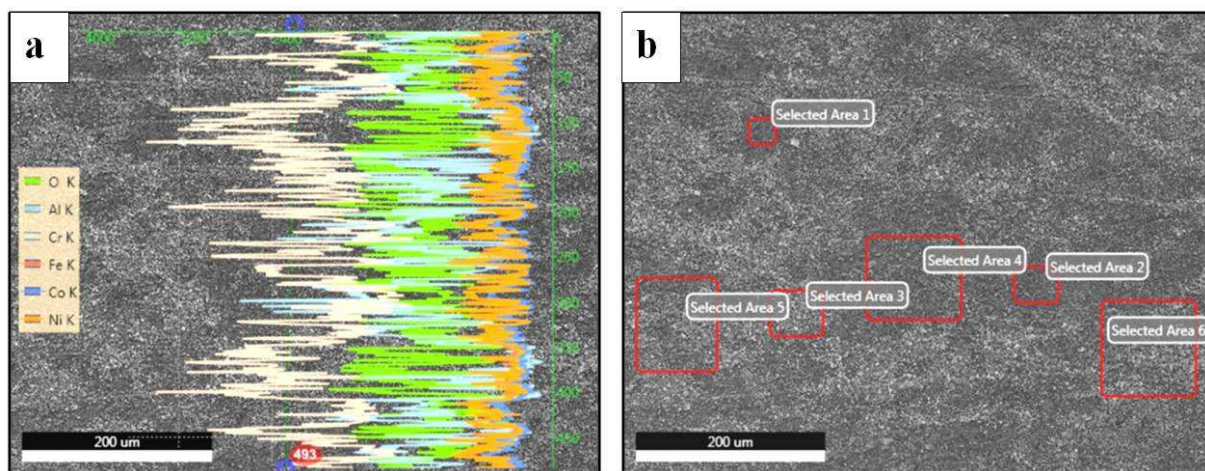
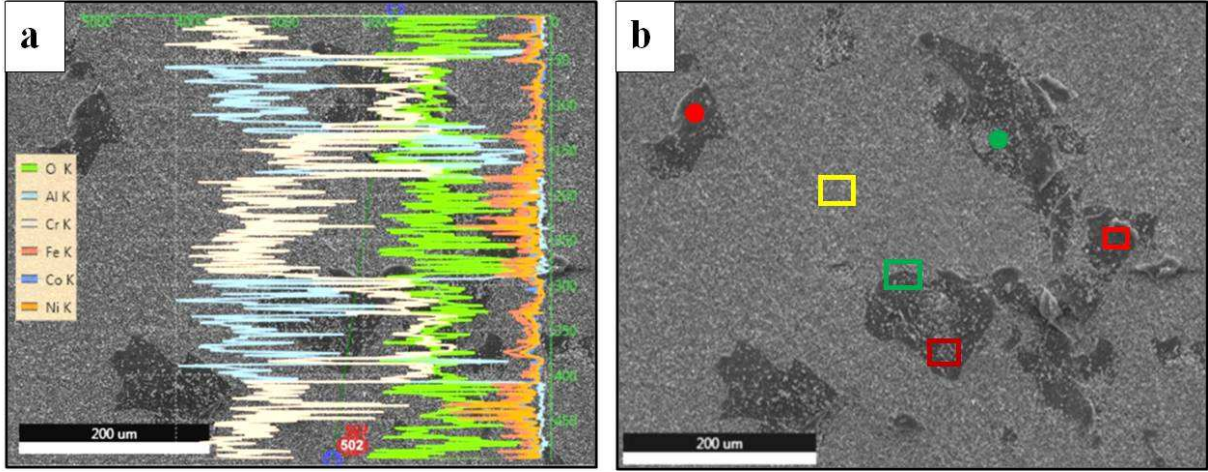


Fig. 17.



Elements	Selected Area 1 (Atomic %)	Selected Area 2 (Atomic %)	Selected Area 3 (Atomic %)	Selected Area 4 (Atomic %)	Selected Area 5 (Atomic %)	Selected Area 6 (Atomic %)
O K	47.97	47.52	43.80	47.82	46.46	46.05
AlK	21.84	22.70	8.77	19.06	13.99	14.15
CrK	12.46	12.46	29.47	16.08	21.46	21.73
FeK	5.53	5.36	5.89	5.37	5.79	5.70
CoK	4.59	4.58	4.61	4.45	4.68	4.66
NiK	7.62	7.39	7.46	7.22	7.63	7.71

Fig. 18.



Elements	Spot 1 ● (Atomic %)	Spot 2 ● (Atomic %)	Selected Area 1 □ (Atomic %)	Selected Area 2 □ (Atomic %)	Selected Area 3 □ (Atomic %)	Selected Area 4 □ (Atomic %)
O K	28.70	33.18	47.24	44.49	39.97	50.23
AlK	35.11	19.18	36.08	23.07	2.33	26.75
CrK	26.36	38.68	14.43	25.19	44.19	15.92
FeK	4.01	4.35	0.73	3.01	5.68	3.07
CoK	2.50	1.86	0.65	1.99	3.55	1.75
NiK	3.32	2.76	0.87	2.25	4.29	2.28

Fig. 19.

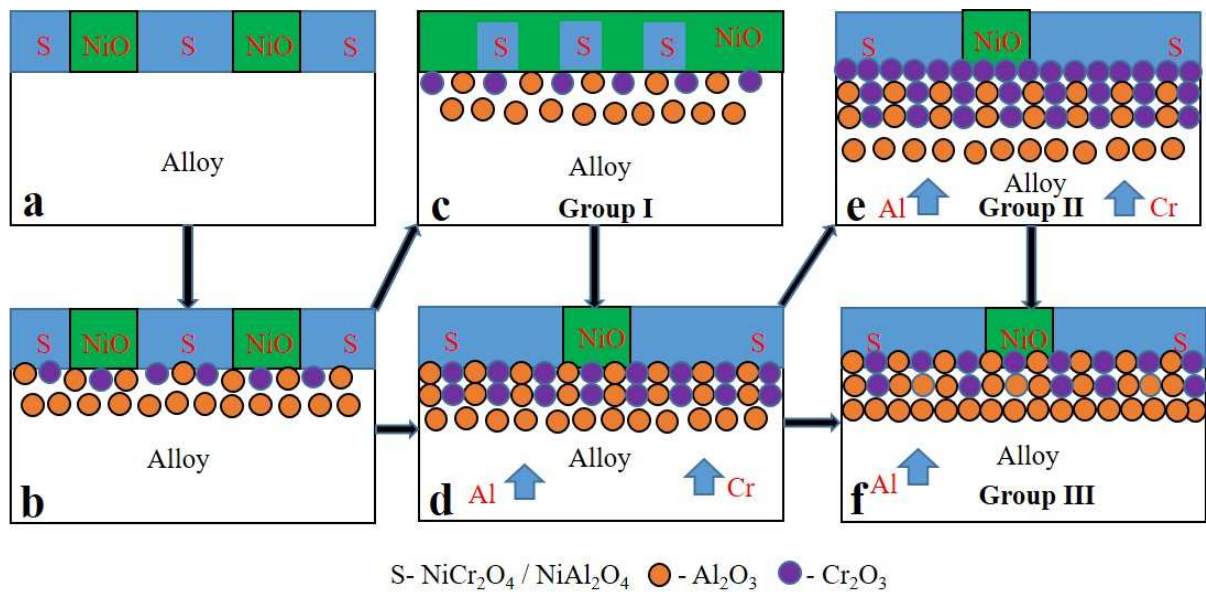


Fig. 20.